

OCTCube: A 3D foundation model for optical coherence tomography that improves cross-dataset, cross-disease, cross-device and cross-modality analysis.

Zixuan Liu¹, Hanwen Xu¹, Addie Woicik¹, Linda G. Shapiro¹, Marian Blazes^{2,3}, Yue Wu^{2,3}, Cecilia S. Lee^{2,3}, Aaron Y. Lee^{2,3}[#], Sheng Wang¹[#]

¹Paul G. Allen School of Computer Science and Engineering, University of Washington, Seattle, WA

²Department of Ophthalmology, University of Washington, Seattle, WA, USA

³Roger and Angie Karalis Johnson Retina Center, University of Washington, Seattle, WA, USA

[#]Email: leeay@uw.edu , swang@cs.washington.edu

Abstract

Optical coherence tomography (OCT) has become critical for diagnosing retinal diseases as it enables 3D images of the retina and optic nerve. OCT acquisition is fast, non-invasive, affordable, and scalable. Due to its broad applicability, massive numbers of OCT images have been accumulated in routine exams, making it possible to train large-scale foundation models that can generalize to various diagnostic tasks using OCT images. Nevertheless, existing foundation models for OCT only consider 2D image slices, overlooking the rich 3D structure. Here, we present OCTCube, a 3D foundation model pre-trained on 26,605 3D OCT volumes encompassing 1.62 million 2D OCT images. OCTCube is developed based on 3D masked autoencoders and exploits FlashAttention to reduce the larger GPU memory usage caused by modeling 3D volumes. OCTCube outperforms 2D models when predicting 8 retinal diseases in both inductive and cross-dataset settings, indicating that utilizing the 3D structure in the model instead of 2D data results in significant improvement. OCTCube further shows superior performance on cross-device prediction and when predicting systemic diseases, such as diabetes and hypertension, further demonstrating its strong generalizability. Finally, we propose a contrastive-self-supervised-learning-based OCT-IR pre-training framework (COIP) for cross-modality analysis on OCT and infrared retinal (IR) images, where the OCT volumes are embedded using OCTCube. We demonstrate that COIP enables accurate alignment between OCT and IR *en face* images. Collectively, OCTCube, a 3D OCT foundation model, demonstrates significantly better performance against 2D models on 27 out of 29 tasks and comparable performance on the other two tasks, paving the way for AI-based retinal disease diagnosis.

Introduction

Optical coherence tomography (OCT) is a non-invasive imaging technique that enables 3D volumetric imaging of the microstructure of the retina.¹ Because OCT images allow clinicians to see the distinctive layers of retina and quantify the thickness of these layers, OCT imaging has become critical for the diagnostic assessments and treatments of many retinal diseases,² including glaucoma,³ diabetic macular edema,⁴ age-related macular degeneration,⁵ referable diabetic retinopathy,^{6,7} retinal neovascularization,⁸ as well as macular hole,⁹ central retinal artery, and vein occlusion.^{10,11} Manual interpretation and analysis of each OCT image in a volume is not only time-consuming but also prone to human error, necessitating the development of automated algorithms and machine learning models to enhance accuracy and efficiency in clinical practice.¹²

Meanwhile, since OCT images are being rapidly accumulated in routine clinical practice, it is possible to develop machine learning models to automate disease diagnosis from OCT images. In particular, image processing techniques, such as contrast-limited adaptive histogram equalization (CLAHE),¹³ speckle noise reduction,¹⁴ layer delineation,¹⁵ and layer segmentation,^{16,17} and deep learning approaches, such as convolutional neural networks,^{5,18,19} generative adversarial networks²⁰ and vision transformers,²¹ have been exploited to develop supervised learning models for OCT-based diagnosis. Recently, foundation models have achieved state-of-the-art performance on various biomedical applications, especially on modeling biomedical images.^{22–24} Foundation models exploit self-supervised learning to learn high-quality representations using large-scale unannotated images and then use these representations to train classifiers for various downstream applications using limited annotations. Recently, RETFound²⁵ has been proposed as a retinal foundation model, which is trained on 1.6 million 2D retinal images including 736,442 2D OCT images (foveal and OCT volume center slice B-scans) and achieves state-of-the-art performance in the prediction of retinal diseases.²⁶ In addition, this foundation model was able to predict several systemic diseases such as myocardial infarction and ischemic strokes.²⁶ However, despite their encouraging performance, existing approaches including RETFound focus on 2D OCT images, overlooking the 3D structure of an OCT volume.²⁷ Modeling the 3D volume has shown to be more effective than 2D images in other medical imaging modalities,^{28–31} such as CT and MRI, by capturing continuous spatial patterns across nearby slices. The opportunity is particularly substantial for OCT imaging as the diseased macular areas might expand across the 3-dimensional spatial region across the fovea.^{32,33} Thus, modeling 3D OCT structure provides both front forward *en face* and depth information, holding the promise to not only improve retinal disease diagnosis and prognosis but also a wide variety of systemic diseases.

Nevertheless, it remains unclear how to computationally model the 3D volume, as simply aggregating predictions slice-by-slice could lead to suboptimal results.³⁴

Here, we present OCTCube, the first 3D foundation model for OCT imaging. OCTCube is trained on 26,605 OCT volumes containing 1.62 million 2D OCT images. The key idea of OCTCube is to model the 3D structure holistically rather than aggregating the information from each 2D slice. Specifically, OCTCube is developed based on 3D masked autoencoders (MAE),^{35–37} where a large proportion of 3D cubes are randomly masked from the OCT volume and then the model is trained to recover these cubes using an encoder-decoder structure (**Fig. 1a**). The encoder is used to initialize specific models for downstream tasks while the decoder is discarded and replaced by the task-specific decoders. In contrast to 2D MAE³⁷ for 2D OCT patches,²⁵ a 3D OCT volume introduces a much longer sequence of cubes, thus presenting much larger GPU memory consumption.³⁸ To address this problem, we exploit FlashAttention^{39,40} to reduce the computational cost, enabling us to efficiently train OCTCube using large-scale 3D volumes. We hypothesize that OCTCube is a broadly applicable and generalizable foundation model for various datasets, diseases and devices by effectively modeling 3D OCT volumes.

We evaluated OCTCube on cross-dataset, cross-disease, cross-modality and cross-device setting to validate its prediction accuracy and generalizability. In prediction of retinal diseases, OCTCube improved average AUPRC from 0.77 to 0.81 in the inductive setting and from 0.66 to 0.77 in the cross-dataset setting compared to 2D model RETFound. On a more challenging cross-device setting, OCTCube significantly outperformed 2D models in analyzing OCT volumes acquired with Topcon Maestro 2 devices while the pre-training data were acquired using Heidelberg Spectralis devices.⁴¹ Next, we found that OCTCube is also able to accurately predict seven different systemic diseases, including diabetes and hypertension. Finally, we extended OCTCube for a cross-modality analysis by developing a novel contrastive self-supervised learning framework named COIP that jointly aligns OCT and IR images, where OCT volumes are embedded using OCTCube. We found that OCTCube achieved better cross-modal retrieval results, serving as the foundation for multi-modal 3D retina modeling. Collectively, we present OCTCube, a 3D foundation model for optical coherence tomography, and demonstrate significant improvement over 2D models on 27 out of 29 tasks (**Fig. 1b**, **Supplementary Fig. 1**), paving the way for AI-based retinal disease diagnosis and prognosis.

Results

Overview of OCTCube

OCTCube is a foundation model pre-trained using 26,605 3D OCT volumes. The key idea of OCTCube is to model the 3D structure holistically instead of aggregating the features from each

2D slice (**Fig. 1a**). To achieve this, OCTCube exploits 3D masked autoencoders as the pre-training framework. In particular, OCTCube first splits an OCT volume into small 3D cubes. It then randomly masks 90% of cubes and uses an encoder-decoder architecture to reconstruct these masked cubes. By training this encoder-decoder architecture using 26,605 OCT volumes, OCTCube is able to obtain a high-quality encoder that can derive accurate representations for a new OCT volume. The decoder will be discarded for downstream applications while the parameters of the encoder will be updated for each downstream task according to the task-specific annotations, such as disease labels. We hypothesize that OCTCube is a broadly applicable and generalizable foundation model for various datasets, diseases and devices by effectively modeling 3D OCT volumes. We evaluate OCTCube on 29 tasks spanning retinal disease prediction, cross-dataset prediction, systemic disease prediction, cross-device prediction and cross-modality analysis (**Fig. 1b**, **Supplementary Fig. 1**). OCTCube attains the significantly best performance on 27 out of 29 tasks and comparable performance on the other two tasks.

Proof-of-concept evaluation of 3D modeling over 2D

As a proof-of-concept to show the benefits of 3D modeling over 2D modeling, we calculated the similarity between two slices in the same OCT volume. We found that nearby slices are more similar in terms of root mean square error (RMSE) (**Supplementary Fig. 2a**) and structural similarity index measure (SSIM) (**Supplementary Fig. 2b**), indicating the presence of repetitive patterns between nearby slices, suggesting the opportunities to exploit slices around the center slice to enhance the signal-to-noise ratio. To verify this, we used RETFound to assign a disease probability of Age-related Macular Degeneration (AMD) for each slice. We then aggregated the predictions from k slices around the center slice by averaging their predicted probabilities (**Supplementary Fig. 3c**). When k is 0, this aggregation approach is the same as a 2D model that only considers the center slice. We found that the best AUROC and the best AUPRC were achieved when k was 14 and 10 respectively, indicating that considering more slices can boost the prediction performance (**Fig. 1c**). We observed similar patterns on seven other retinal diseases (**Supplementary Fig. 4**). Moreover, because RETFound is pre-trained and fine-tuned only using center OCT slices, when all slices are considered ($k=60$), the prediction performance could be worse than when only considering center slices. Furthermore, the efficacy of a 3D model that simply averages the predicted probability of all slices is compromised, as many diseases develop and progress at different locations and rates. This variability highlights the need for a more advanced 3D approach that can adapt to different disease areas.

To further support this conclusion, we present case studies of two AMD patients (**Fig. 1d,e**, **Supplementary Fig. 5a,b**) who were both predicted incorrectly as non-AMD patients by RETFound using the center slice (slice 30). In contrast, OCTCube used other nearby slices to predict AMD as drusens, small deposits in the retina, were observed in these slices and

highlighted as the source of prediction by the corresponding saliency maps (**Fig. 1d,e**, **Supplementary Figs. 5c,d, 6-7**).

Retinal disease prediction in the inductive learning setting

We first evaluated OCTCube on the prediction of eight retinal diseases, including Primary Open-Angle Glaucoma (POAG), Diabetic Macular Edema (DME), Age-related Macular Degeneration (AMD), Epiretinal Membrane or Macular Hole (ERM/MH), Diabetic Retinopathy without Macular Edema (DR), Central Artery / Vein Retinal Occlusion (CRAO/CRVO), Posterior Vitreous Detachment (PVD) and Retinal Neovascularization (RNV). We exploited 5-fold cross validation settings with 20% data (**Fig. 2a-b**) and 80% data (**Supplementary Figs. 8-9**) to fine-tune our pretrained model for each disease. We set the pre-training patient collection, the fine-tuning patient collection, and the test patient collection to be independent from each other to ensure a practical inductive learning setting. We first compared OCTCube to supervised models that did not leverage unannotated images for pre-training and found that OCTCube substantially outperformed them with an average 53.8% AUPRC and 45.4% AUROC relative improvement, indicating the importance of pre-training. RETFound, which is pre-trained on 2D images, also outperformed supervised models, reemphasizing the effectiveness of pre-training. Next, we assessed the advantage of considering the entire 3D volumes by comparing OCTCube to RetFound (center), which uses the embedding of the center slice, and RETFound (all), which averages the embeddings of slices in the same volume (**Supplementary Fig. 2a,b**). We found that OCTCube significantly outperformed both variants of RETFound on 7 out of the 8 diseases (paired t-test p-value < 1e-3). Since our method and RETFound are both developed based on MAE, the superior performance of our method demonstrates the effectiveness of modeling the 3D volume. The improvement of OCTCube is more prominent on POAG among the eight diseases. Because POAG diagnosis relies on measuring the change of layer thickness throughout the entire macula, requiring the global context of the full volume at the same time to determine the diagnosis,⁴² this larger improvement further reveals OCTCube's ability to leverage retinal patterns beyond the fovea. Interestingly, the supervised (all) model did not outperform the supervised (center) model, suggesting that the benefit of 3D modeling mostly arose from the pre-training stage. In conclusion, our experiments on eight retinal disease predictions in the inductive learning setting demonstrate the effectiveness of OCTCube by leveraging the 3D structure of OCT volumes.

To further understand the improvement of OCTCube, we visualized the saliency maps of an AMD patient on multiple slices around the center slice, reflecting the image regions that the model used to make the prediction (**Fig. 2c-f**). We first found that both OCTCube and RETFound capture relevant clinicopathologic features such as the drusen to predict AMD.

Nevertheless, OCTCube utilized consistent regions across slices, while RETFound used relatively different regions across slices, suggesting that OCTCube considers the 3D spatial fundus structure. We further visualized the saliency map of the OCT volume across the slow-scan dimension (**Supplementary Fig. 10**), and again observed clinically relevant saliency maps generated by OCTCube at the level of the retinal pigment epithelium in the perifoveal region. In contrast, RETFound demonstrated less meaningful saliency maps in this dimension partially due to its pre-training only using the slow-scan and depth dimension, indicating the broad applicability of OCTCube to analyze OCT images from different dimensions.

Cross-dataset and cross-device prediction

The superior performance on OCTCube motivates us to benchmark it on independent datasets that neither RETFound nor OCTCube has access to in the pre-training stage, enabling us to more rigorously examine the impact of the 3D model under potential population variance and batch effects. We evaluated different methods on five independent datasets (**Fig. 3a-b, Supplementary Fig. 11**). Similar to our observation on the UW Ophthalmology dataset, we found that OCTCube outperformed 2D models with a large margin (16.8% AUPRC improvement). RETFound (all) also outperformed Retfound (center), highlighting the effectiveness of considering the entire 3D volume. Importantly, our method still outperformed RETFound (all) by 8.5% AUPRC and 6.9% AUROC improvement, demonstrating the effectiveness of 3D pre-training. Collectively, OCTCube significantly outperformed both variants of RETFound on 4 out of the 5 datasets, demonstrating that OCTCube could be a broadly applicable tool for retinal disease prediction.

Since independent datasets might have varying numbers of annotated data, we next investigated the performance of OCTCube under different ratios of training data (**Fig. 3c,d**). We found that while OCTCube achieved the best performance on different training data ratios, its improvement was larger when there are fewer annotations, indicating its superiority in the low-resource setting. For example, RETFound (center) achieves 0.86 AUROC that is comparable to OCTCube (0.87 AUROC) using 70% of training data, but its performance drops substantially to 0.61 AUROC when only using 20% of training data, whereas OCTCube still maintains a good AUROC of 0.77.

Finally, we examined a more challenging task of cross-device prediction (**Fig. 3e,f**), where the test data at the fine-tuning stage are collected from Topcon Maestro 2 devices⁴¹ in the AI-READI dataset.⁴³ RETFound was trained on Topcon 3D OCT-2000 SA devices⁴⁴ and Topcon Triton devices,⁴¹ while OCTCube was trained solely on the more difference Heidelberg Spectralis devices.⁴⁵ A few examples of images acquired by these different devices are illustrated in **Supplementary Fig. 12**, showing clear visual distinctions between the same OCT volume from

different devices. Even though RETFound was trained on Topcon images and OCTCube was not, we found that OCTCube significantly outperformed RETFound (center) by 29.3% AUPRC and RETFound (all) by 4.3% AUPRC on the Topcon test images, demonstrating its strong generalizability across datasets and across devices.

Prediction on systemic diseases

After confirming the performance of OCTCube on predicting retinal diseases, we next investigated whether OCTCube can be used to predict systemic diseases related to retinal structure by exploiting OCT volumes. We selected 7 diseases based on International Statistical Classification of Diseases (ICD-9⁴⁶ and ICD-10^{47,48}) codes that are frequently found among people with retinal conditions. Among them, hypertension was diagnosed in 3,440 patients, occurring in 35% of the patients with disease records included in our study, diabetes was diagnosed in 2,420 patients, occurring in 24.7% of the included patients. We found that OCTCube significantly outperformed RETFound on 5 out of 7 disease labels in terms of AUPRC (**Fig. 4a**) and 7 out of 7 in terms of AUROC (**Fig. 4b**) on predicting concurrent systemic diseases, demonstrating the advantage of modeling 3D OCT volumes for predicting systemic diseases.

To further understand how OCTCube successfully predicts systemic diseases, we examined the performance of the aggregation approach (**Supplementary Fig. 3c**) that averages the prediction scores over multiple slices (**Fig. 4c**, **Supplementary Fig. 13**). We found that aggregating more slices can improve the prediction performance on all seven diseases, necessitating the modeling of 3D structures. Moreover, the improvement of OCTCube over RETFound (center) and the improvement of the aggregation approach over RETFound (center) are highly correlated (Pearson correlation 0.86 for AUROC and 0.78 for AUPRC), indicating that both methods leverage similar 3D patterns to enhance the prediction performance (**Fig. 4d,e**). Nevertheless, OCTCube consistently outperformed the aggregation approach under various numbers of slices, demonstrating its effectiveness in modeling 3D structures.

Since OCTCube achieved the largest improvement on predicting diabetes diagnosis, we have included a case study of a patient with diabetes to understand how OCTCube leverages OCT volumes for diabetes prediction (**Fig. 4f-h**). We observed many hard exudates, indicators of early diabetic retinopathy, present in various OCT scans of the right eye (**Fig. 4f**). However, hard exudates were not present in the center slice (slice 30). As a result, OCTCube was able to predict diabetic retinopathy but RETFound could not based on the OCT scans of the right eye. In contrast, a larger burden of hard exudates were found in the OCT scans of the left eye (**Fig. 4g**, **Supplementary Fig. 14**) as well as in both eyes during the 1 year follow up visit (**Fig. 4h**, **Supplementary Fig. 15**). The hard exudates are more severe in the left eye (OS) on the same acquired date and in the right eye acquired during the one-year follow-up visit, therefore both

OCTCube and RETFound correctly predicted the diagnosis of diabetes in these instances. In conclusion, RETFound can only make correct predictions when patterns are visible and present on the center slice, whereas OCTCube is able to correctly predict diabetes when patterns are less visible on a single slice, leading to potential early disease detection.

Cross-modality analysis of OCT and IR images through contrastive self-supervised learning

Finally, we investigated whether OCTCube as an OCT-based foundation model can be integrated with Infrared Retinal (IR) imaging modality. IR is usually taken together with the OCT imaging as the navigation map and provides a much larger 2D *en face* field of vision (FOV) of multiple fundus components,⁴⁵ such as optic disc, vessel direction, and the projected structure of macula. In practice, it is challenging and tedious to jointly analyze OCT volumes and IR pairs even for human experts.⁴⁹ Therefore, we sought to investigate whether OCTCube could help learn a shared embedding space by aligning OCT and IR images. To this end, we collected 26,605 IR images for the same patient population and studied two retrieval tasks: find the most relevant OCT volume given an IR image and vice versa. Since 3D MAE pre-training does not directly provide cross-modal representation, we propose COIP, a contrastive self-supervised learning-based OCT-IR pre-training framework, to align these two modalities in a joint embedding space (**Fig. 5a,b**, see **Methods**). We found that OCTCube is able to retrieve relevant images across modalities more accurately with a 0.64 Recall@1, substantially higher than the 0.46 Recall@1 attained by RETFound, indicating the effectiveness of OCTCube on aligning OCT and IR images. RETFound (all) also outperformed RETFound (center), again demonstrating the benefits of modeling OCT data in the 3D space for multi-modal analysis (**Fig. 5c,d**, **Supplementary Fig. 16a,b**). Next, we studied the retrieval performance on AI-READI where the alignment of both RETFound and OCTCube were fine-tuned using the UW Ophthalmology dataset. OCTCube again outperformed RETFound (all) and RETFound (center) on both retrieving OCT to IR and IR to OCT, and the improvement was much larger on this cross-dataset setting, indicating its wide applicability to cross-modality analysis. Furthermore, we used laterality to evaluate this cross-modality alignment by examining whether OCTCube can retrieve images with the same laterality (right (OD) or left (OS) eye). OCTCube achieved the best performance on both IR to OCT and OCT to IR laterality prediction with an average 0.97 accuracy@1 (**Fig. 5e,f**, **Supplementary Fig. 16c,d**). Finally, we selected four case studies from the UW Ophthalmology (**Fig. 5g,h**) and AI-READI⁴³ (**Fig. 5i,j**) datasets and found that the improvement of OCTCube came from successfully matching fundus structure between modalities. For example, OCTCube retrieved similar IR images for the OCT volume that is optic-disc centered (**Fig. 5g**), while both RETFound (all) and RETFound (center) failed to retrieve optic-disc centered IR images. Additional examples showed that OCTCube better understands macular changes and laterality (**Fig. 5h**), illumination difference (**Fig. 5g,h**) and

blood vessel structure (**Fig. 5g,i,j**), demonstrating its ability to capture spatial fundus structures through 3D modeling.

Discussion

OCTCube is related to previous efforts in computational ophthalmology, especially previous works that develop deep learning-based approaches for diagnosing and predicting retinal diseases from OCT images. In particular, previous studies have used deep convolutional neural networks,^{5,7,18,34} generative adversarial networks,^{10,20} multimodal feature learning⁴ and anomalies detection² to predict diabetic retinopathy, diabetic macular edema, age-related macular degeneration and glaucoma. In contrast to these approaches, OCTCube has been developed as a foundation model using self-supervised learning, which consists of a pre-training stage and a fine-tuning stage. As a result, unlabeled images can be utilized by OCTCube to provide accurate initialization for the supervised fine-tuning stage. OCTCube is inspired by RetFound, the first foundation model for OCT images. In contrast to RetFound, OCTCube directly modeled the 3D structure of OCT volumes. Our extensive experiments show that OCTCube outperforms RetFound in various settings, demonstrating the importance of 3D volumes.

There are a few limitations we would like to address for OCTCube in future work. First, we hope to explore how to jointly train multi-modal^{4,52-54} 3D foundation models for additional types of retinal images beyond OCT and IR, such as fundus autofluorescence (FAF),⁵⁵ color fundus photography (CFP)⁵⁶ and Fluorescein Angiography (FA)⁵⁷ images. By jointly modeling all of the imaging modalities, especially in the 3D space, we could more comprehensively characterize the retina, thus deriving more robust performance for downstream applications. However, it remains unclear how to computationally integrate all of them given the computational cost and unmatched modality structures. Second, despite being equipped with the interpretable method, OCTCube could be more clinically useful if we are able to identify the most important cubes that contribute to the final disease predictions and filter out less important cubes to improve efficiency. We plan to explore advanced interpretable methods, such as SHAP⁵⁸ and RELPROP,⁵⁹ to identify such cubes and enable better interpretation and efficacy in the future. Third, a retinal patient could have multiple visits, presenting a longitude data containing multiple 3D volumes. We plan to incorporate such temporal information into OCTCube by extending it to 4D space where time is the fourth dimension.^{60,61} While incorporating temporal information into medical imaging foundation models has not been well studied before, we plan to use more computationally efficient neural network architectures to allow the model to consider a time-series of volumes at the same time.

We have developed OCTCube, a 3D foundation model for optical coherence tomography trained from 26,605 3D OCT volumes spanning 1,622,905 2D OCT images. We demonstrate the advantage of modeling 3D volumes holistically instead of pre-training on 2D image sets by comparing OCTCube to 2D OCT foundation models on multiple independent datasets. We found that OCTCube outperformed comparison approaches consistently in all 29 tasks with significant improvement on 27 tasks (**Fig. 1b, Supplementary Fig. 1**), including retinal disease prediction, cross-dataset prediction, cross-device prediction, systemic disease prediction and cross-modality retrieval, indicating its accurate performance and strong generalizability. The strong predictive performance of OCTCube on both retinal diseases and systemic diseases indicates its potentially broad applicability. OCTCube may be used as a general tool for analyzing OCT data, paving the path for AI-based retinal diagnostic and prognostic.^{50,51}

Figure legends

Fig. 1 OCTCube model overview. **a**, OCTCube exploits 3D Masked Autoencoders (MAE) for the pre-training. MAE uses an encoder-decoder architecture where it randomly masks 90% of the cubes in each volume at the encoding stage and is optimized to reconstruct them at the decoding stage. The encoder and the decoder are implemented using a 3D Vision Transformer (ViT). FlashAttention is further used to reduce the GPU memory usage when modeling 3D cubes. **b**, Radar plot comparing the performance of OCTCube and competing methods on 29 tasks, including eight retinal disease prediction tasks in the inductive learning setting, five retinal disease prediction tasks in the inductive learning setting, seven systemic disease prediction tasks, eight cross-modality retrieval tasks and one cross-device prediction task. Recall@1 is used as the metric for the cross-modal retrieval tasks, Acc@1 is used as the metric for the cross-modal laterality prediction tasks, and AUROC is used as the metric for the other tasks. UW-Oph is the abbreviation for UW Ophthalmology dataset. **c**, Plot showing the AUROC and AUPRC of an aggregation approach (**Supplementary Fig. 3c**) averages the prediction probabilities of k slices around the center slices, where k is shown in the x-axis and the prediction probability is derived using RETFound. The metric AUROC and AUPRC are the abbreviation of Area under the Receiver Operating Characteristic Curve and the Area under the Precision-Recall Curve. RETFound, as a 2D approach, corresponds to $k = 0$. **d,e**, Visualization of the center OCT slice (slice 30) and the OCT slice near the center slice, including the corresponding prediction probabilities of two AMD patients (**d** for patient 1 and **e** for patient 2). Red boxes highlight the small drusen that occurs at the slice 31 of patient 1 and the slice 28 of patient 2, indicating signals for AMD.

Fig. 2 Evaluation on retinal disease prediction in the inductive learning setting. **a,b**, Barplots comparing OCTCube and competing methods on disease classification of 8 retinal diseases on UW Ophthalmology dataset in terms of AUPRC (**a**) and AUROC (**b**). Inductive learning setting is used to ensure that test OCT volumes are not seen by OCTCube in the pre-training stage. The train:validation:test split is set to be 20%:60%:20%. POAG, DME, AMD, ERM/MH, DR, CRAO/CRVO, PVD, RNV denote primary open-angle glaucoma, diabetic macular edema, age-related macular degeneration, epiretinal membrane or macular hole, diabetic retinopathy without macular edema, central retinal vein / artery occlusion, posterior vitreous detachment, and retinal neovascularization, respectively. Supervised approaches do not have a pre-training stage. RETFound (all) and Supervised (all) average the embeddings of all slices within a 3D volume. * indicates the significance level at which OCTCube outperforms the best-competing method, with paired t-test p-value $< 5 \times 10^{-2}$ for *, p-value $< 1 \times 10^{-2}$ for **, p-value $< 1 \times 10^{-3}$ for ***. **c-f**, Visualization of multiple slices across the slow-scan dimension from a single OCT volume with the sampling location (**c**) in the corresponding IR en face image, OCT slices (**d**), saliency

maps based on the prediction of RETFound (center) (e), and saliency maps based on the prediction of OCTCube (f). OCTCube provides a more coherent saliency map across slices in the diseased area, indicating the effectiveness of the 3D modeling. Red lines in (a) are drawn with the consideration of pixel spacing of sampled OCT slices. Red pixels in (e,f) indicate higher importance determined by the model, while blue pixels indicate lower importance. Images are resized to (256, 256) for visualization.

Fig. 3 Evaluation on cross-dataset and cross-device prediction. a,b, Barplots comparing OCTCube and competing methods on predicting retinal disease in terms of AUPRC (a) and AUROC (b) in the cross-dataset setting. OCTCube is trained on UW Ophthalmology dataset while the testing OCT volumes are collected from five other independent datasets. c,d, Plots comparing OCTCube and competing methods across different ratios of fine-tuning data in terms of AUROC (c) and AUPRC (d). e,f, Barplots comparing OCTCube and competing methods in the cross-device setting in terms of AUROC (e) and AUPRC (f). OCTCube is trained on UW Ophthalmology images collected on Heidelberg Spectralis while test volumes are collected on Topcon Maestro 2 devices from the AI-READI dataset. * indicates the significance level at which OCTCube outperforms the best-competing method, with paired t-test p-value $< 5 \times 10^{-2}$ for *, p-value $< 1 \times 10^{-2}$ for **, p-value $< 1 \times 10^{-3}$ for ***.

Fig. 4 Evaluation on systemic disease prediction. a,b, Barplots comparing OCTCube and competing methods on predicting seven systemic diseases in the UW Ophthalmology dataset in terms of AUPRC (a) and AUROC (b). Inductive learning setting is used to ensure that test OCT volumes are not seen by OCTCube in the pre-training stage. * indicates the significance level at which OCTCube outperforms the best-competing method, with paired t-test p-value $< 5 \times 10^{-2}$ for *, p-value $< 1 \times 10^{-2}$ for **, p-value $< 1 \times 10^{-3}$ for ***. c, Plots showing the AUPRC performance of an aggregation approach that averages the predicted probabilities of k slices around the center slices on seven systemic diseases, where k is shown in the x-axis. The prediction probability is derived using RETFound. The RETFound (center) model, as a 2D approach, corresponds to $k = 0$ (Supplementary Fig. 3a). Different from directly averaging predictions, the RETFound (all) model uses a neural network to aggregate features (Supplementary Fig. 3b). The improved performance by considering more slices necessitates the development of 3D models. d,e, Scatter plots comparing the relative improvement over RETFound (center) by OCTCube and by the aggregation approach in terms of AUROC (d) and AUPRC (e) across seven diseases. The high Pearson correlation indicates that the improvement of OCTCube is from considering the 3D structure. f, Visualization of OCT slices from the right eye (OD) of the patient with diabetes at the first visit. Hard exudates are observed in several slices (marked by red boxes) but are not clearly seen in the center slice. RETFound thus failed to predict diabetes by only using the center slice. In contrast, OCTCube successfully predicted

diabetes with probability of 0.72 by considering the entire volume. **g,h**, Visualization of representative OCT slices from the left eye (OS) acquired at the same day (**g**) and the right eye acquired after 1 year (**h**) for the same patient. Macular edema and hard exudates can be observed more clearly compared to the slices in OD (**f**), indicating diabetic retinopathy. RETFound successfully predicts diabetes using the center slice of OS (**g**) and OD 1 year (**h**), but fails using OD (**f**). In contrast, OCTCube successfully predicts diabetes using either OS, OD, or OD 1 year.

Fig. 5 Evaluation on cross-modality analysis. **a**, Illustration of the cross-modality alignment using COIP, a novel contrastive self-supervised learning-based framework for integrating OCT and IR modalities, after the 3D MAE pre-training. COIP utilized contrastive loss to align 3D OCT volume and IR *en face* image pairs. OCTCube is used to initialize the OCT encoder and RETFound is used to initialize the IR encoder. **b**, Illustration of cross-modality retrieval evaluation. After the alignment, the OCT to IR retrieval task is evaluated by retrieving the most similar IR image based on the queried OCT volume. The IR to OCT retrieval task is evaluated similarly. **c-d**, Barplots comparing OCTCube and competing methods on cross-modality retrieval on UW Ophthalmology and cross-AI-READI dataset in terms of recall@1 (**c**) and recall@5 (**d**) score on OCT to IR retrieval and IR to OCT retrieval. * indicates the significance level at which OCTCube outperforms the best-competing method, with paired t-test p-value $< 5 \times 10^{-2}$ for *, p-value $< 1 \times 10^{-2}$ for **, p-value $< 1 \times 10^{-3}$ for ***. **e-f** Barplots comparing OCTCube and competing methods on cross-modality laterality prediction on UW Ophthalmology and AI-READI dataset in terms of accuracy@1 (**e**) and accuracy@5 (**f**) on OCT to IR retrieval and IR to OCT retrieval. * indicates the significance level at which OCTCube outperforms the best-competing method, with paired t-test p-value $< 5 \times 10^{-2}$ for *, p-value $< 1 \times 10^{-2}$ for **, p-value $< 1 \times 10^{-3}$ for ***. **g-j**, Visualization of the top retrieved IR images given four different queried OCT volumes. Ground truth IR images are excluded. OCTCube retrieves more similar images that have similar structures in the retina, such as the optic disc (**g**), macula changes and lateralities (**h**), illumination difference (**g,h**) and blood vessels (**g,i,j**).

Methods

Details of UW Ophthalmology dataset

Dataset overview. The UW Ophthalmology dataset contains 3D macula OCT volumes, paired Infrared Retinal images from the medical screening process of 17,214 patients, along with the diagnosis codes (ICD-9 and ICD-10 code) across the UW-medicine system. In this study, we utilize this dataset for pre-training, within-dataset ophthalmic disease prediction, systemic cross-disease prediction, and cross-modality prediction. We only include the first screening of each patient, to avoid distribution shifts brought by the longitudinal follow-up screening results. We include data samples from both eyes of a patient when available. This results in 33,262 3D OCT volume and IR image pairs. Each macula OCT volume and its paired IR images were extracted by the Heidelberg Spectralis (Heidelberg Engineering) imaging device⁴⁵ from 2006 to 2023. The IR images are not used in the pre-training stage and only used for the cross-modality analysis. Each OCT volume is a composition of either 60 or 61 slices, and the default digital resolution of each slice is 496 by 768. The absolute pixel spacing varies for each dimension and each instance, and the average pixel spacing area is 7.51 by 1.88 by 8.66 mm. The paired IR image is taken together with the OCT volume acquisition, and the typical digital resolution is 768 by 768. This study was approved by the Institutional Review Board of the University of Washington (UW) and was in adherence with the tenets of the Declaration of Helsinki and the Health Insurance Portability and Accountability Act.

Data split. We split the dataset at patient level, with a ratio of 80% training and 20% test for the within-dataset evaluation. This results in 26,605 training and 6657 test sample volumes from 13,771 and 3,443 patients. For all the conducted experiments, the held out test set is only used for evaluation. In the pre-training stage, only the 3D macula OCT volumes are included and associated disease labels for these volumes are not seen by the model. In the within-dataset retinal and systemic cross-disease prediction, the OCT volumes are used to predict diagnosis information provided as label supervision. In the cross-modality prediction, both the OCT volumes and IR images are provided to perform alignment training and evaluation. Among all 17,214 patients, 12,830 patients had clinical records available. We thus use this subset to construct the data for the within-dataset retinal and systemic cross-disease prediction task.

Labels for retinal disease prediction. We picked 8 retinal diseases based on ICD code (**Supplementary Fig. 17, Supplementary Table 1**): Primary Open-Angle Glaucoma (POAG, 1,248 patients), Diabetic Macular Edema (DME, 881 patients), Age-related Macular Degeneration (AMD, 1,888 patients), , Diabetic Retinopathy without Macular Edema (DR, 1,694 patients), Epiretinal Membrane or Macular Hole (ERM/MH, 1,482 patients), Central Retinal Artery or Vein Occlusion (CRAO/CRVO, 204 patients), Posterior Vitreous Detachment (PVD,

1,725 patients), Retinal Neovascularization (RNV, 299 patients). We then set up the rest of the recorded patients as the non-diseased cohort (3,936 patients). We also included patients with multiple retinal diseases, resulting in a multi-label and imbalanced dataset. We followed the train-test set split in the pre-training stage to hold out the test samples that are not seen in the pre-training stage for evaluation. For all the tasks being evaluated, we further split the training subset into train and validation subsets as 75% to 25%, resulting in a data split of 60% training, 20% validation, 20% test split.

Labels for systemic cross-disease prediction. We aimed to examine if OCTCube is able to predict other systemic diseases using OCT volumes. We extracted the ICD code of systemic diseases for the recorded patients and counted their frequencies. We merged ICD-9 code to ICD-10 code and used the first level code of the ICD-10 code system. We then extracted all the level 1 disease codes with frequency larger than 100, resulting in 455 different diseases over 9,801 patients. The disease distribution can be seen at (**Supplementary Fig. 18**). We used these samples to construct the multi-label systemic cross-disease dataset. We followed the same train and validation split as we did in preparing data for retinal disease prediction, ensuring samples in the held out test set are never seen in the pre-training stage.

Details of OCTCube

Detailed overview of OCTCube. In this section we present the detailed architecture, design, and training of the OCTCube. OCTCube is based on attention-based Vision Transformer, which treats OCT volumes as a long sequence of continuous cube feature vectors and learns to generate summarized representations from the sequence based on stacked multi-head attention and non-linear transformations. It is composed of a heavy transformer encoder and a lightweight transformer decoder, and is trained with 3D masked autoencoder objectives.³⁵ The encoder first indexes the spatial position of each cube, and then randomly selects most of the cube tokens and masks them out from the long sequences, and processes the rest feature sequence together with their indexed position information. After getting the output from the encoder, the lightweight decoder will insert a learnable embedding vector named <mask> as the placeholder token for each masked-out cube at its original indexed position and try to reconstruct the whole sequence. The reconstruction is guided by minimizing the mean squared error (MSE), thus not requiring label supervision at all. Prior works³⁵⁻³⁷ have shown that this process will lead to a good encoder for downstream tasks. After the training, the decoder will be discarded and the encoder is taken as the basic encoder for the downstream tasks.

Decomposing the volume into the sequence of 3D cubes. Unlike a plain 2D Vision Transformer,³⁸ the OCTCube is a designated 3D-aware Vision Transformer model that can take 3D OCT volumes or 2D OCT slices with arbitrary sizes. To achieve this, OCTCube utilizes

CubeEmbed, a non-overlapped 3D convolution layer that can split the OCT volumes into small cubes and project each cube to an embedding token vector. Let (z, h, w) be the cube size pre-chosen in the CubeEmbed layer, applying this operation to the whole 3D OCT volume with Z slices and (H, W) resolution will result in a long sequence of cube embedding with length of $(Z * H * W) / (z * h * w)$. It is thus crucial to pick an appropriate cube size in order to both maintain flexibility and avoid heavy computation. For the OCT modality, we propose to use a smaller size on the 3rd z -axis and a larger window size on the 2D slices for three reasons. First, depending on the scanning mode, the z -axis might have a much sparser sampling region; a smaller z will lead to similar pixel spacing to the other two dimensions. Second, a smaller z will provide flexibility to handle volumes with less number of slices. To the extreme, 2D slices can be treated as the volume with $z=1$, and since the slices will commonly be converted to a duplicated 3-channel rgb image, we set the cube size to be 3 in OCTCube. This makes OCTCube capable of taking both 2D slices and 3D volumes as inputs, improving its flexibility on downstream applications. We also make a 2D positional embedding for the h and w axis and a separate positional embedding for the 3rd z -axis, to help the model adapt to variant volume size. What's more, setting $z=3$ has another important benefit to accelerate the learning, which is being easy to utilize pre-trained 2D checkpoints to warm up the 3D-aware model, with simple conversion from PatchEmbed to CubeEmbed. This allows OCTCube to quickly adapt from 2D to 3D with much less computation effort.

Incorporating FlashAttention into OCTCube. One big drawback of 3D modeling in medical imaging is the drastically increased computational cost. Compared to the pure convolutional neural network, the plain vision transformer suffers more on the increased sequence length, as the multi-head attention induces $O(L^2)$ space and time complexity, where L is the sequence length. As an example, an OCT volume with resize resolution $48 \times 256 \times 256$ with cube size $3 \times 16 \times 16$ leads to a sequence with length of 4,096, and fine-tuning a ViT-large encoder with a linear projection head with this single sequence will used up more than 50 GB GPU memory, which exceeds the memory of most of the GPUs. To relieve this issue and make OCTCube more efficient and affordable to end users, we incorporate FlashAttention-2^{39,40} into the Vision Transformer structure. FlashAttention-2 is an advanced technology that helps to reduce the GPU memory costs by 5~20 times and enable 2~4x training / inference speed for transformer structure without accuracy lost, by optimizing the computation of attention. Because FlashAttention-2 reduces the space complexity of attention from $O(L^2)$ to $O(L)$, including FlashAttention-2 reduces the GPU memory usage of the above example to 10.52 GB, which is more affordable on modern GPUs. Moreover, the computing speed also achieves at least 2 times improvement. This greatly improves the efficiency of OCTCube.

Prediction head design. In the fine-tuning stage for downstream tasks, a light weight multi-layer perceptron (MLP) head is used to map the representation of the OCT volumes to the outcome.

After getting the output representation sequence from the pre-trained encoder, we perform average pooling for representation at all spatial positions and acquire the overall embedding. We use slightly different heads for disease prediction tasks and the cross-modality prediction task.

For the disease prediction tasks, we use a MLP layer with layer normalization to map the representation to the number of classes, depending on the tasks. Dropout^{38,62} is set for all disease prediction experiments with a rate of 0.5 to avoid over-fitting. For the cross-modality prediction tasks, the dropout operation is removed for full feature utilization. We add one more MLP layer with the same dimension of the embedding dimension, and a GELU⁶³ non-linear activation to map the representation to the aligned space.

Extending RETFound to handle 3D OCT volumes. The original RETFound encoder only takes 2D OCT slices as input (referred to as RETFound (center)). We extend RETFound to handle 3D OCT volumes in a multi-instance learning manner: Given an OCT volume with size (Z, H, W), we input all Z slices into the RETFound and acquire the embedding for each slice. We then aggregate the embedding together with average pooling for the final representation of the volumes (referred to as RETFound (all)). We maintain the prediction head design to be the same as OCTCube for these two major baselines for a fair comparison.

Another critical change we made for RETFound is to equip the model also with FlashAttention-2. Without such modifications, RETFound will fail in most of the experiments. Interestingly, we observe that, when equipped with FlashAttention-2, RETFound (all) will consume more GPU memory when taking the same size of OCT volumes. This is because OCTCube can better benefit from the space complexity improvement in terms of sequence length, as it takes the whole volume as a single sequence. On the other hand, the extended RETFound is equivalent to multi-slice learning with a large batch size of short slice sequence. This makes the OCTCube encoder not only capable of leveraging information across the volume, but also able to enjoy higher computational efficiency. As an example, fine tuning a 48 by 256 by 256 OCT volume with the OCTCube encoder will take less than 25 GB GPU memory, while the RETFound model with FlashAttention-2 will take more than 60.52 GB GPU memory.

Pre-training data processing and other implementation details. For the 3D OCT volume data for pre-training OCTCube, we resize the images to 60 by 256 by 256. We then normalize the voxel to the region of 0 to 1. We perform very lightweight augmentation, such as random flip. We discard the ImageNet mean and standard deviation normalization as the 3D OCT volumes do not have 3 channels and only do [0, 1]-normalization. We set the cube size to be 3 by 16 by 16, this gives sequences with length of in total 20 by 16 by 16 = 5,120. We therefore set up the 2D position embedding to be the shape of 16 by 16, and the z-axis position embedding length to be 20.

We set up the encoder of OCTCube to be ViT-large, with 24 layers, 16-heads and 1024-dim embedding for each layer, and the decoder to be ViT-small, with 8 layers, 16-heads and 512-dim embedding for each layer. Different from RETFound, we used a mask ratio of 90%, as it has been proved to be an optimal setting in 3D MAE training.³⁵ As discussed before, setting $z=3$ enables us to borrow from other pretrained 2D checkpoints. We therefore set up the RETFound OCT ViT-large model as the initialized checkpoint, with moderate modification. We trained OCTCube using a batch size of 4 (effective 2D batch size = 240) on 4 NVIDIA A100 80 GB devices with 50 epochs. We used the AdamW optimizer with a base learning rate of 1.6×10^{-3} with cosine annealing. The first 5 epochs are set to be the warm up epochs with a linear increase of lr from 0 to the peak learning rate. The whole training usually takes 5 days.

Details of within-dataset retinal disease prediction

We formulate the disease prediction of the eight diseases as eight binary classification tasks, and a multi-task setting by jointly predicting all eight diseases. For the binary disease prediction, the non-diseased cohort is treated as the negative controls. For the multi-task setting, the non-diseased cohort is treated as the negative controls for all diseases. For each disease, only patients with the record of the matched disease code were included in the training and the evaluation. For each experiment, we trained the model for 10 epochs with a learning rate of 5×10^{-3} and a batch size of 1, and applied the learning rate warming up (from 0 to 5×10^{-3}) strategy to the first epoch and a cosine annealing schedule for the rest of the epochs. Similar to the setting used by RETFound, we performed label smoothing with smoothing factor 0.1. The validation set is used to perform model selection, where the model with highest AUPRC will be used for evaluation on the held out test set. For the RETFound (center) model, only the center slice was extracted from the OCT volume and served as the input. We set up the batch size to be 16 and the number of epochs to be 50, following the original RETFound setting for a fair comparison. For the transformer encoder, we set up layer-wise learning rate decay with a factor of 0.65, to achieve better trade-off between utilizing learnings from the pre-training in the early

layers and flexible weight adjustment for downstream tasks in the layers close to the prediction head.

For the interpretable visualization of OCTCube and RETFound (center), we leveraged gradient-based visualization to better understand the pixel-level importance to disease prediction, instead of visualizing the attention map that only assigns importance at patch or cube level. Specifically, we chose Grad-CAM++⁶⁴ as the base method, which utilizes second-order gradients to help generate saliency maps. We adopted Pytorch-grad-cam software⁶⁵ to instantiate Grad-CAM++ for both OCTCube and RETFound (center). For RETFound (center), since the prediction was made based on each slice, a saliency map would thus be generated when hooking the model with the visualization method. For OCTCube, directly hooking the software did not work, because the prediction was made based on the whole volume. We therefore adapted the software to allow gradient flow pass through the 3D-aware ViT and reorganized the shape to generate saliency map for each slice, or for the other perspective that visualizes depth and slice sampling direction. For the slice perspective, we visualized the saliency map on the slice with a resized resolution of 256 by 256. For the other perspective, we adjusted the image from 61 by 496 to 61 by 256 and then visualized the saliency map with adjustment of aspect ratio to view it as a 256 by 256 image. We used the grayscale saliency and converted the intensity distribution to color distribution using the software for better visualization. For the sampling location and pixel spacing of each OCT slice on IR image (marked as red line), we extracted such information from the metadata of the imaging process and removed the out-of-FOV sampling region. We used a red line with different linewidth to denote the real pixel spacing in different directions, as the slice perspective usually has larger pixel spacing compared to the other perspective.

Details of cross-dataset and cross-device prediction

We leverage 6 public cross-sectional 3D OCT volumetric disease datasets for cross-dataset and cross-device evaluation. These datasets target on multiple ophthalmological and systemic, such as Age-related Macular Degeneration (AMD), Glaucoma, Diabetic Macular Edema (DME), multi-stage Macular Hole (MH), Multiple Sclerosis (MS), and Type-2 Diabetes Mellitus (T2DM). We formatted the disease prediction task on these datasets as binary or categorical classification depending on the number of classes. We summarized the datasets below:

UMN dataset⁶⁶: This dataset contains 29 patients with DME and 24 patients with AMD. OCTCube is used to predict binary classification. The number of slices for each volume is 25, and the digital resolution is 496 x 1024. Each slice is resized to 256 x 256 for the downstream evaluation.

DUKE 14 dataset^{66,67}: This dataset contains in total 45 patients either being healthy, with AMD, or with DME. Each class has 15 patients. OCTCube is used to predict 3-class classification. The

number of slices for each volume is 50, and the digital resolution is 496×512 . Each slice is resized to 256×256 for the downstream evaluation.

HCMS dataset⁶⁸: This dataset contains 14 healthy patients and 21 patients with multiple sclerosis. OCTCube is used to predict binary classification. The number of slices for each volume is 49, and the digital resolution is 496×1024 . Each slice is resized to 256×256 for the downstream evaluation.

Glaucoma dataset⁴²: This dataset contains in total 1,110 Patients, where 263 of them are healthy, and the rest 847 of them are with glaucoma. OCTCube is used to predict binary classification. The number of slices for each volume is 64, and the digital resolution is 128×64 . Each slice is resized to 128×128 for the downstream evaluation.

OIMHS dataset⁹: This dataset contains in total 3,859 OCT slices extracted from 125 eyes of 118 patients that have either 4 stages of macular holes. We exclude the stage 1 class because the number of patients is 1. Among the rest, 16 volumes are with stage 2, 34 volumes are with stage 3 and 74 volumes are with stage 4. OCTCube is used to predict 3-class stage classification. The screening of each eye results in a 3D OCT volume with a variant number of slices from 17 to 97. For the evaluation on this dataset, we picked up the number of slices to be included for each volume as 17. For the digital resolution, 220 images has a resolution of 384×496 pixels, 3002 images has a resolution of 512×496 pixels, and 637 images has a resolution of 768×496 pixels. Each slice is resized to 256×256 for the downstream evaluation.

AI-READI dataset⁴³: This dataset is a recently-released flagship dataset focusing on Type 2 Diabetes Mellitus. The current released version (v1.0.0) is cross-sectional and contains 204 patients, with 4 diagnosis outcomes: healthy (74 patients), pre-diabetes (48 patients), Type-2 diabetes with oral medication and/or non insulin injectable medication controlled (57 patients), Insulin-dependent T2DM (25 patients). We used the OCT volumes dataset acquired by TopCon Maestro 2 imaging devices to test the cross-device disease prediction performance. For the cross-device disease prediction task, we clustered healthy and pre-diabetes patients into one group, and the other two diabetes-diagnosed into another, and then performed binary classification between these two groups. The resulting control and diseased group size are 122 and 78, respectively. The number of slices for each volume is 128, and the digital resolution is 885×512 . We filter out patients with problematic z-axis coherence and missing data, resulting in 167 patients included, resulting in 330 OCT volumes.

For all the public datasets except DUKE14, we set up multi-fold splits to evaluate the effectiveness of OCTCube. We first seek to investigate OCTCube's performance at label-restricted situations. We first set up 10-fold splits for UMN, HCMS, Glaucoma, and OIMHS. For this type of split, we perform training using only 1 fold (10% data as training), and evaluate the performance on the rest of the 90% subset. For DUKE 14, we do a 5 fold split and use 20% data as a training set, as 10% training data can not always include all three classes into

every split. We then turn to understand the model performance at label-rich situations. We only study and report HCMS, Glaucoma, OIMHS and AI-READI for this situation, as both the RETFound and OCTCube achieve almost perfect performance on DUKE14 and UMN in this situation. We set up a standard 5-fold cross validation for this setting, where for each iteration, one of the folds will be treated as the validation set, and the other four folds will be treated as the training set.

For the data ratio ablation study on OIMHS dataset, we use k% of the data to be set as the training set. We set up k% to be 10%, 20%, 30%, 40%, 50%, 60%, 70%, and 80%. For each k, we randomly select 5 splits based on the ratio and report the validation performance. For the cross-device study on AI-READI dataset, we utilize the same split for dataset from all three devices. Because the pixel spacing, intensity distribution and sampling frequency on three axes are different across device type and settings, we perform a pixel spacing adjustment for data taken by Topcon Maestro 2 and Topcon Triton devices as OCTCube is pre-trained on data taken from Heidelberg Spectralis device. Specifically, we perform foreground extraction on the y-axis (the depth axis) using the OTSU filter⁶⁹ across the volume to adjust the pixel spacing. We then perform intensity thresholding to ground the extreme dark and light pixels. For each volume, We set up the pixel value at 1×10^{-4} and 0.9999 percentile to be the grounding pixel value, the pixel smaller or larger than the threshold will be converted to the threshold, respectively. This helps to adjust the intensity distribution to be more aligned with the intensity distribution of the pre-trained dataset. We then interpolate the z-axis to 60 to align with the pre-training data distribution, as well as reducing the computational cost brought by the large z-axis sampling frequency. For the RETFound (center) and 3D baselines on the cross-device disease prediction experiments on AI-READI, we found the models achieve inferior performance (slightly better than random) with standard [0,1]-normalization for the data collected by Topcon Maestro 2 devices. We therefore specifically adjust the normalization to be both [0,1]-normalization and ImageNet normalization to help not cover their potential. It is worth noting that we didn't encounter this problem when experimenting with other datasets.

For the modeling training, we set up a longer training recipe for the public dataset, with in total 100 epochs and 10 epochs for warming up the learning rate from 0 to the peak, as the dataset size is relatively smaller. We follow the similar setting as we did in the within-dataset retinal disease prediction.

Details of systemic cross-disease prediction

We set up the multi-label task using the constructed ICD10-based disease labels. We did not utilize any other prior knowledge about diseases that are correlated with retina, but directly leveraged OCTCube to extract possible predictable signals. Specifically, we used the same training recipe as we did in the within-dataset retinal disease prediction. We calculated the macro AUROC and AUPRC over all classes and used this macro AUPRC for model selection.

After picking up the best checkpoint, we calculated the class-wise metrics over all 455 diseases, and found out the diseases that have predictable signals. We reported the 7 diseases that have balanced accuracy significantly higher than 0.5 (measured by two-sided t-test) using the best checkpoint. They are Diabetes (E11), Hypertension (I10), Joint pain (M25), Hyperlipidemia (E78), Soft tissue disorders (M79), Back pain (M54), and general Pain (G69). Diseases such as diabetes and hypertension have been shown to have correlation with various retinopathy, validating our prediction signal extraction process.

Details of disease prediction by extending and aggregating slices

For the feature aggregation study presented in **Fig. 4c-e** and **Supplementary Fig. 3,11**, we extracted the logits of the selected diseases from the RETFound (center) model for all the slices of all volumes in the held out test set. We then performed the prediction aggregation, by averaging the prediction of k slices besides the center slice (slice 30) in both directions. A choice of k indicates an aggregation of predictions from $2k + 1$ slices. We reported the standard deviation based on 5 runs of RETFound (center) model, and reported the mean value of OCTCube and RETFound (all) model (the same as in **Fig. 2a-b** and **Fig. 4a-b**). We calculated the correlation between the relative improvements brought by aggregation and OCTCube and reported the Pearson correlation coefficient. Both correlation achieved a p-value < 0.05 .

Details of cross modality alignment

COIP: Contrastive OCT volume-IR image pre-training. Given an OCT volume and its paired IR image, it is challenging to measure the similarity between them from pure vision. Directly compressing OCT to an ‘averaged’ en face map is inferior, as (i) the FOV of OCT volumes is much smaller than the IR image, (ii) discrepancies between OCT slices might exist, and (iii) some detailed structures such as vessel might be missing after the compression. While modern imaging devices such as the Heidelberg Spectralis imaging device may provide scanning coordinates in IR image for each OCT slice, it’s challenging to incorporate such anchoring information into multimodal representation learning. One key challenge is that the unsupervised self mask-and-reconstruct 2D / 3D MAE objectives used to pre-train OCTCube are not directly applicable for the cross-modal analysis. We therefore propose COIP, a large-scale contrastive learning strategy at the volume-image level between OCT volume and IR images, on the UW Ophthalmology dataset. COIP is different from 2D or 3D MAE, serving as a secondary representation learning procedure after the first-stage pre-training. The idea of COIP is inspired by Contrastive language-image pre-training (CLIP),⁷⁰ which tries to learn a multimodal embedding space by pushing positive image-text pairs together, and pulling the negative image-text apart. The key advantage of this method is the contrastive loss being used only requires positive-negative pair information, which is naturally lied in the OCT-IR pair datasets. We thus replace the image-text design with 3D OCT volume--2D IR image and propose COIP.

Given a batch of N (OCT, IR) pairs, COIP aims to train two separate encoders Enc_O and Enc_I for each modality. Let O_j and I_j be the embedding of the j -th OCT volume and IR image pair output by the encoder,, COIP optimize the symmetric cross-entropy style INFONCE⁷¹ loss:

$$\mathcal{L} = -\frac{1}{2N} \left(\sum_{i=1}^N \log \frac{e^{\cos(O_j, I_j)/\tau}}{\sum_{k=1}^N e^{\cos(O_j, I_k)/\tau}} + \sum_{i=1}^N \log \frac{e^{\cos(O_j, I_j)/\tau}}{\sum_{k=1}^N e^{\cos(O_k, I_j)/\tau}} \right)$$

Here, $\cos(O_j, I_k)$ is the cosine similarity of the j -th OCT embedding O_j and the k -th IR embedding I_k , τ is a learnable scaling temperature factor.

Adapting OCTCube to boost COIP. We aim to evaluate how OCTCube will help COIP training. Specifically, we set the initial OCT volume encoder to be the pre-trained encoder of OCTCube. Directly setting Vision Transformer as the OCT volume encoder has several computational challenges. First, the sequence length of the 3D volume will be much longer. Second, the InfoNCE loss used in COIP suggests a large batch size, this prerequisites brings extra constraint for the GPU space consumption. As an example, the original OCTCube with fully fine-tunable weights can only use a batch size of 8 on a NVIDIA A100 GPU. To relieve this challenge, we make a critical modification to adapt OCTCube for affordable and efficient COIP training. Specifically, we set up a more aggressive layer-wise learning rate decay strategy by freezing the first two third layers (in total 16) of the transformer encoder and layer decay of 0.65 for the last 8 layers. This makes the actual gpu memory consumption to be only at most one third of the original cost, providing a more efficient training recipe. It is worth noting that such strategy, being compromised to sup-optimal performance compared to using a fully fine-tunable model, is much less harmful to OCTCube, thanks to the 3D MAE pre-training. For the RETFound baselines, we make the strategy the same for a fair comparison. We maintain the volume size to be $60 \times 256 \times 256$, the same as what we have done in the 3D MAE pre-training.

Other implementation details. COIP was developed based on an open sourced distributed contrastive language-image pre-training (OpenCLIP)⁷² based on PyTorch.⁷³ We performed moderate adaptation to set up two image encoders for COIP.

Since our goal is to understand how well OCTCube is as the base OCT volume encoder, for the IR image encoder, we chose not to pre-train on IR images but directly use the ViT-large model checkpoint trained on Color Fundus Photography by RETFound, to serve as a relatively acceptable initialization for IR images. We set up the IR encoder to be fully fine-tunable, in order not to restrict the COIP model with sub-optimal IR embedding. We set up the IR image resolution to be 224×224 , following the original design of RETFound.

For the training recipe, we wanted to validate the hypothesis that OCTCube has captured meaningful embeddings for OCT volumes. We therefore set up a relatively short 50 epoch

training procedure. We used the AdamW optimizer, set the learning rate to be 1×10^{-4} , and linear warming up steps to be 200.

We further optimized the GPU memory cost with several techniques, namely gradient checkpointing, automatic mixed precision (AMP) with float16 (whenever possible) and sharded contrastive loss, which provides identical gradient, but removes redundant intermediate cross-GPU similarities computation and only computes similarities between local relevant features. All of these improvements led to an achievable single-GPU batch size of 32 on 4 NVIDIA A100 80GB GPUs. To further enlarge the effective batch size, we set up an accumulated gradient with a step of 4, resulting in a batch size of 512 over all GPUs. We maintained the setting of RETFound baselines to be the same. The whole training usually takes less than 2 days.

Evaluation of COIP within UW Ophthalmology dataset. We evaluated the retrieval performance of COIP on the held out test set as discussed before. Following the protocol of previous work,⁷⁴ we performed cosine similarity based nearest neighbor search at the whole test set level, i.e., retrieval from in total 6,647 images / volumes. Given a test set with size of T , we first computed the embedding of all OCT volumes and IR images in the test set, respectively. We then calculated the pairwise cosine similarity of all pairs, resulting in a $T \times T$ similarity matrix. Given an OCT volume embedding, the top- K most similar IR embedding will be retrieved, and vice versa. We then reported top- K recall (referred to as $R@K$), which counts if the correct paired images / volumes are within the top- K retrieved list. Besides, we report mean rank, i.e., the average ranking of the ground-truth images / volumes. We performed sub-training and sub-validation splits similar to what we did previously and used the validation subset for model selection. The best model checkpoint was picked based on the average of the $R@1$ for both modalities on the validation set. For the zero-shot laterality retrieval task, we removed the ground truth from the candidate list to better understand if the embedding space is able to cluster images / volumes by laterality. For each query IR image / OCT volume, we retrieve the volumes / images with top- K similarity to calculate the accuracy@ K ($Acc@K$), by computing how many of them have the same laterality compared to the query.

Evaluation of COIP cross AI-READI dataset. For the cross-dataset multimodal alignment task, we leveraged the Heidelberg Spectralis OCT-IR paired subset from AI-READI dataset to test the cross-dataset multimodal alignment performance. The Heidelberg Spectralis OCT-IR subset covered almost the same patient cohort compared to the Topcon Maestro 2 subset used in cross-device disease prediction. Among all 204 patients, 172 of them took the data collection process using Heidelberg Spectralis imaging devices. We used all the available 344 macula OCT-IR pairs to construct the cross-dataset test set. For each OCT / IR query sample, the candidate retrieval set is the whole set of the other modality. We set up the preprocessing for

OCT volumes and IR images to be the same as the training pipeline for a fair evaluation. We followed the same evaluation protocol of the within-dataset setting. For the zero-shot laterality retrieval task, we follow the setting used in the evaluation of UW Ophthalmology dataset.

Setting of case study demonstration. For the qualitative case studies reported, we set up the retrieval task of retrieving the most possible IR image given a query OCT volume. Because of the challenges to demonstrate visual similarity of a 3D OCT volume and its paired IR image, we chose to visualize the ground truth IR image for the query. To better understand how different models perform retrieval, we modified the quantitative evaluation protocol discussed above slightly by removing the ground truth paired IR image from the candidate set. While it is impossible to retrieve the correct IR image, the compromised retrieval results reveal the importance of different anatomic structures in the retina for the retrieval, such as the optic disc, blood vessels and their locations / directions, through the lens of qualitative similarity of visual patterns.

Evaluation standards and statistical analysis

For the inhouse retinal and systemic cross-disease prediction tasks, we set up 5 random sub-training and sub-validation splits and report the average performance and standard deviation. For the cross-dataset retinal disease prediction task, we run the 10-fold 10% training data and 5-fold cross validation setting with 3 random splits. We use two-sided t-tests to test OCTCube and the most comparable baseline to show the significance.

Reference

1. Bernardes, R. & Cunha-Vaz, J. *Optical Coherence Tomography: A Clinical and Technical Update*. (Springer Science & Business Media, 2012).
2. Burlina, P., Paul, W., Liu, T. Y. A. & Bressler, N. M. Detecting Anomalies in Retinal Diseases Using Generative, Discriminative, and Self-supervised Deep Learning. *JAMA Ophthalmol.* **140**, 185–189 (2022).
3. Park, K. H. & Kim, T.-W. *OCT Imaging in Glaucoma: A Guide for Practitioners*. (2021).
4. Parravano, M. *et al.* Multimodal imaging in diabetic retinopathy and macular edema: An update about biomarkers. *Surv. Ophthalmol.* (2024) doi:10.1016/j.survophthal.2024.06.006.
5. Li, X., Jia, M., Islam, M. T., Yu, L. & Xing, L. Self-Supervised Feature Learning via Exploiting Multi-Modal Data for Retinal Disease Diagnosis. *IEEE Trans. Med. Imaging* **39**, 4023–4033 (2020).
6. Tao, Y. *et al.* Exploration on OCT biomarker candidate related to macular edema caused by diabetic retinopathy and retinal vein occlusion in SD-OCT images. *Sci. Rep.* **14**, 14317 (2024).
7. Shanthini, A., Manogaran, G. & Vadivu, G. *Deep Convolutional Neural Network for The Prognosis of Diabetic Retinopathy*. (Springer Nature, 2022).
8. Prenner, V. *et al.* Advancing the visibility of outer retinal integrity in neovascular age-related macular degeneration with high-resolution OCT. *Can. J. Ophthalmol.* (2024) doi:10.1016/j.jcjo.2024.05.014.
9. Ye, X. *et al.* OIMHS: An Optical Coherence Tomography Image Dataset Based on Macular Hole Manual Segmentation. *Sci Data* **10**, 769 (2023).

10. Razavi, P. *et al.* Changes in wider field swept-source OCT angiography vascular metrics with anti-vascular endothelial growth factor therapy in central retinal vein occlusion. *Graefes Arch. Clin. Exp. Ophthalmol.* **262**, 2111–2120 (2024).
11. Hong, S. H. & Kim, H. D. Central retinal artery occlusion after intravitreal brolucizumab injection for treatment-naïve neovascular age-related macular degeneration; a case report. *BMC Ophthalmol.* **24**, 200 (2024).
12. De Fauw, J. *et al.* Clinically applicable deep learning for diagnosis and referral in retinal disease. *Nat. Med.* **24**, 1342–1350 (2018).
13. Opoku, M., Weyori, B. A., Adekoya, A. F. & Adu, K. CLAHE-CapsNet: Efficient retina optical coherence tomography classification using capsule networks with contrast limited adaptive histogram equalization. *PLoS One* **18**, e0288663 (2023).
14. Wong, A., Mishra, A., Bizheva, K. & Clausi, D. A. General Bayesian estimation for speckle noise reduction in optical coherence tomography retinal imagery. *Opt. Express* **18**, 8338–8352 (2010).
15. Sun, J. Q. *et al.* Comparison of the Iowa Reference Algorithm to the Heidelberg Spectralis optical coherence tomography segmentation algorithm. *J. Biophotonics* **13**, e201960187 (2020).
16. Garvin, M. K. *et al.* Automated 3-D intraretinal layer segmentation of macular spectral-domain optical coherence tomography images. *IEEE Trans. Med. Imaging* **28**, 1436–1447 (2009).
17. Quellec, G. *et al.* Three-dimensional analysis of retinal layer texture: identification of fluid-filled regions in SD-OCT of the macula. *IEEE Trans. Med. Imaging* **29**, 1321–1330 (2010).

18. Lee, C. S., Baughman, D. M. & Lee, A. Y. Deep learning is effective for the classification of OCT images of normal versus Age-related Macular Degeneration. *Ophthalmol Retina* **1**, 322–327 (2017).
19. Li, Q. *et al.* DeepRetina: Layer Segmentation of Retina in OCT Images Using Deep Learning. *Transl. Vis. Sci. Technol.* **9**, 61 (2020).
20. Sun, L.-C. *et al.* Generative adversarial network-based deep learning approach in classification of retinal conditions with optical coherence tomography images. *Graefes Arch. Clin. Exp. Ophthalmol.* **261**, 1399–1412 (2023).
21. Cai, L. *et al.* Classification of diabetic maculopathy based on optical coherence tomography images using a Vision Transformer model. *BMJ Open Ophthalmol* **8**, (2023).
22. Ikezogwo, W. O. *et al.* Quilt-1M: One Million Image-Text Pairs for Histopathology. *Adv. Neural Inf. Process. Syst.* **36**, 37995–38017 (2023).
23. Xu, H. *et al.* A whole-slide foundation model for digital pathology from real-world data. *Nature* **630**, 181–188 (2024).
24. Huang, Z., Bianchi, F., Yuksekgonul, M., Montine, T. J. & Zou, J. A visual-language foundation model for pathology image analysis using medical Twitter. *Nat. Med.* **29**, 2307–2316 (2023).
25. Zhou, Y. *et al.* A foundation model for generalizable disease detection from retinal images. *Nature* **622**, 156–163 (2023).
26. Zhang, J. *et al.* RETFound-enhanced community-based fundus disease screening: real-world evidence and decision curve analysis. *NPJ Digit Med* **7**, 108 (2024).
27. Curcio, C. A., Kar, D., Owsley, C., Sloan, K. R. & Ach, T. Age-Related Macular

- Degeneration, a Mathematically Tractable Disease. *Invest. Ophthalmol. Vis. Sci.* **65**, 4 (2024).
28. Wang, H. *et al.* SAM-Med3D. *arXiv [cs.CV]* Preprint at <http://arxiv.org/abs/2310.15161> (2023).
 29. Blankemeier, L. *et al.* Merlin: A vision language foundation model for 3D computed tomography. *arXiv preprint arXiv:2406.06512* (2024).
 30. Wang, G. *et al.* MIS-FM: 3D medical image segmentation using foundation models pretrained on a large-scale unannotated dataset. *ArXiv* **abs/2306.16925**, (2023).
 31. Hamamci, I. E. *et al.* A foundation model utilizing chest CT volumes and radiology reports for supervised-level zero-shot detection of abnormalities. *arXiv [cs.CV]* (2024).
 32. Lin, A. C., Lee, C. S., Blazes, M., Lee, A. Y. & Gorin, M. B. Assessing the Clinical Utility of Expanded Macular OCTs Using Machine Learning. *Transl. Vis. Sci. Technol.* **10**, 32 (2021).
 33. Park, S.-J., Ko, T., Park, C.-K., Kim, Y.-C. & Choi, I.-Y. Deep Learning Model Based on 3D Optical Coherence Tomography Images for the Automated Detection of Pathologic Myopia. *Diagnostics (Basel)* **12**, (2022).
 34. Rasel, R. K. *et al.* Assessing the efficacy of 2D and 3D CNN algorithms in OCT-based glaucoma detection. *Sci. Rep.* **14**, 11758 (2024).
 35. Feichtenhofer, C., Fan, H., Li, Y. & He, K. Masked Autoencoders As Spatiotemporal Learners. *Adv. Neural Inf. Process. Syst.* **abs/2205.09113**, (2022).
 36. Tong, Z., Song, Y., Wang, J. & Wang, L. VideoMAE: Masked autoencoders are data-efficient learners for self-supervised video pre-training. *Adv. Neural Inf. Process. Syst.* **abs/2203.12602**, (2022).
 37. He, K. *et al.* Masked autoencoders are scalable vision learners. in *Proceedings of the IEEE/CVF conference on computer vision and pattern recognition* 16000–16009 (2022).

38. Dosovitskiy, A. *et al.* An image is worth 16x16 words: Transformers for image recognition at scale. *Int Conf Learn Represent* **abs/2010.11929**, (2020).
39. Dao, T., Fu, D. Y., Ermon, S., Rudra, A. & R'e, C. FlashAttention: Fast and memory-efficient exact attention with IO-awareness. *Adv. Neural Inf. Process. Syst.* **abs/2205.14135**, (2022).
40. Dao, T. FlashAttention-2: Faster attention with better parallelism and work partitioning. *ArXiv* **abs/2307.08691**, (2023).
41. Ko, T. H., Chisholm, C. M. & Chen, M. H. 11. Optical coherence tomography angiography imaging on the Topcon Triton and Maestro2 systems. *Optical Coherence Tomography Angiography of the Eye* (2024).
42. Maetschke, S. *et al.* A feature agnostic approach for glaucoma detection in OCT volumes. *PLoS One* **14**, e0219126 (2019).
43. AI-READI Consortium. Flagship dataset of type 2 diabetes from the AI-READI project. FAIRhub <https://doi.org/10.34534/1> (2024).
44. Chen, B., Chen, H., Zheng, C. & Zhang, M. Performance of Topcon 3D optical coherence tomography-2000 in re-analyzing OCT-1000 raw data. *Exp. Ther. Med.* **17**, 4395–4402 (2019).
45. Barteselli, G. *et al.* Accuracy of the Heidelberg Spectralis in the alignment between near-infrared image and tomographic scan in a model eye: a multicenter study. *Am. J. Ophthalmol.* **156**, 588–592 (2013).
46. Buck, C. J. *2015 ICD-9-CM for Hospitals, Volumes 1, 2 and 3 Standard Edition - E-Book*. (Elsevier Health Sciences, 2015).
47. Cartwright, D. J. ICD-9-CM to ICD-10-CM Codes: What? Why? How? *Adv. Wound Care* **2**, 588–592 (2013).

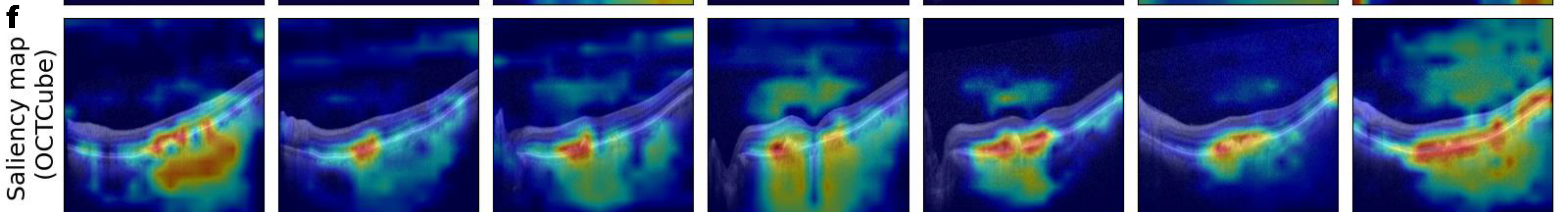
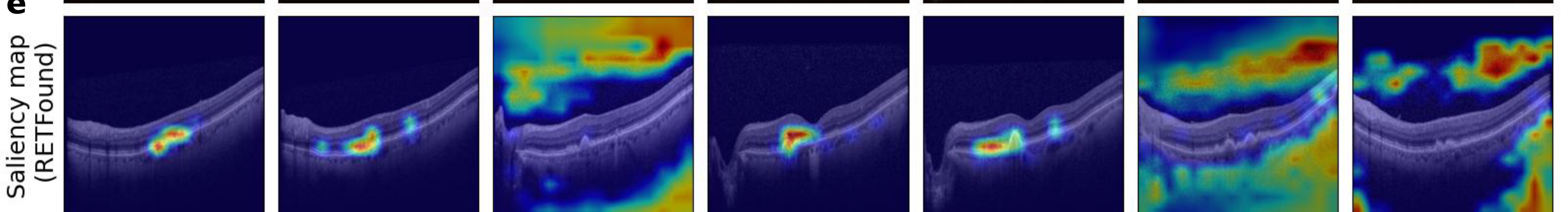
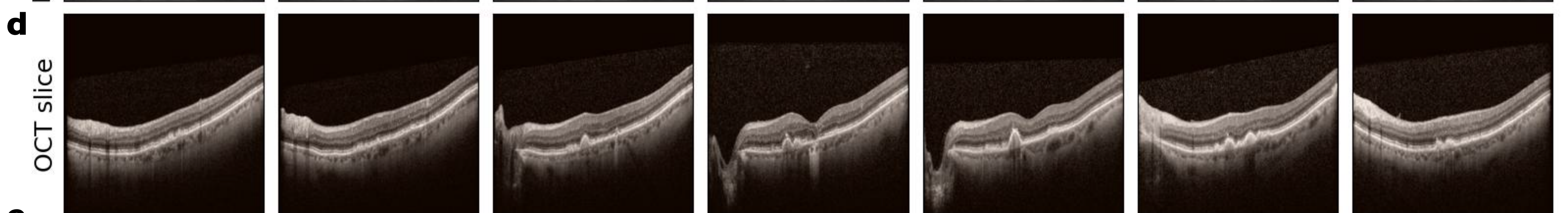
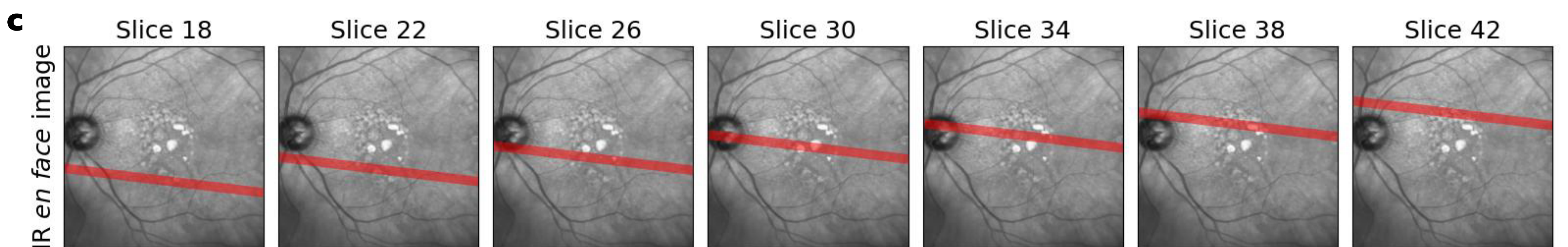
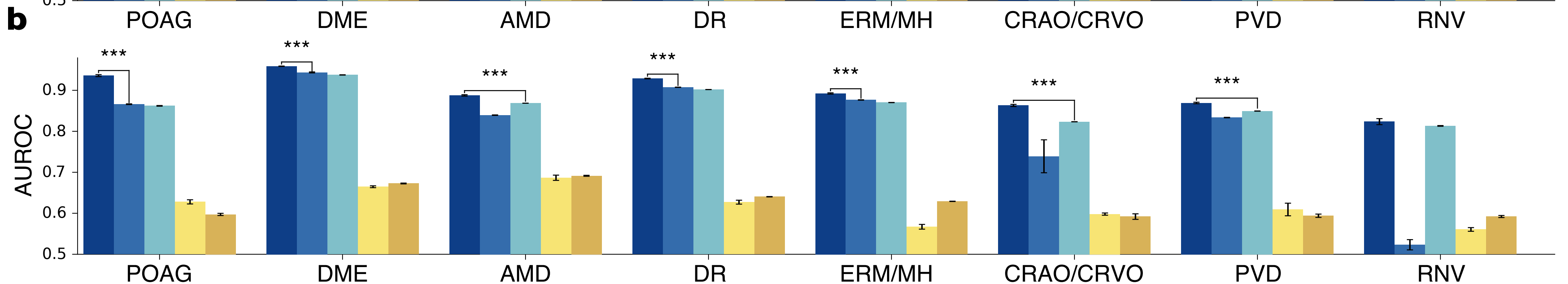
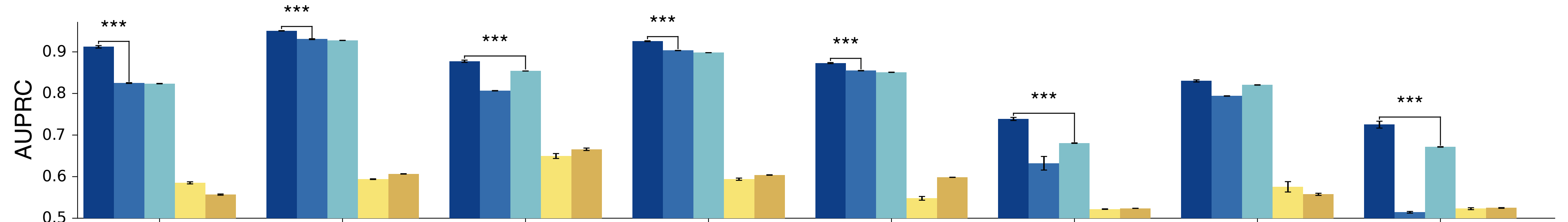
48. American Medical Association. *ICD-10-CM 2020 the Complete Official Codebook*. (American Medical Association Press, 2019).
49. Chen, M. *et al.* Automated diagnosis of age-related macular degeneration using multi-modal vertical plane feature fusion via deep learning. *Med. Phys.* **49**, 2324–2333 (2022).
50. Grzybowski, A. *Artificial Intelligence in Ophthalmology*. (Springer Nature, 2021).
51. Ting, D. *et al.* Artificial intelligence and deep learning in ophthalmology. *Br. J. Ophthalmol.* **103**, 167–175 (2018).
52. Zhao, H. *et al.* MMICL: Empowering Vision-language Model with Multi-Modal In-Context Learning. *arXiv [cs.CL]* (2023).
53. Li, C. *et al.* Llava-med: Training a large language-and-vision assistant for biomedicine in one day. *Adv. Neural Inf. Process. Syst.* **36**, (2024).
54. Wu, R. *et al.* MM-Retinal: Knowledge-enhanced foundational pretraining with Fundus Image-text expertise. *ArXiv* **abs/2405.11793**, (2024).
55. Spaide, T. *et al.* Geographic Atrophy Segmentation Using Multimodal Deep Learning. *Transl. Vis. Sci. Technol.* **12**, 10 (2023).
56. Niemeijer, M., van Ginneken, B., Staal, J., Suttorp-Schulten, M. S. A. & Abràmoff, M. D. Automatic detection of red lesions in digital color fundus photographs. *IEEE Trans. Med. Imaging* **24**, 584–592 (2005).
57. Fernando Arévalo, J. *Retinal Angiography and Optical Coherence Tomography*. (Springer Science & Business Media, 2008).
58. Lundberg, S. M. & Lee, S.-I. A unified approach to interpreting model predictions. *Adv.*

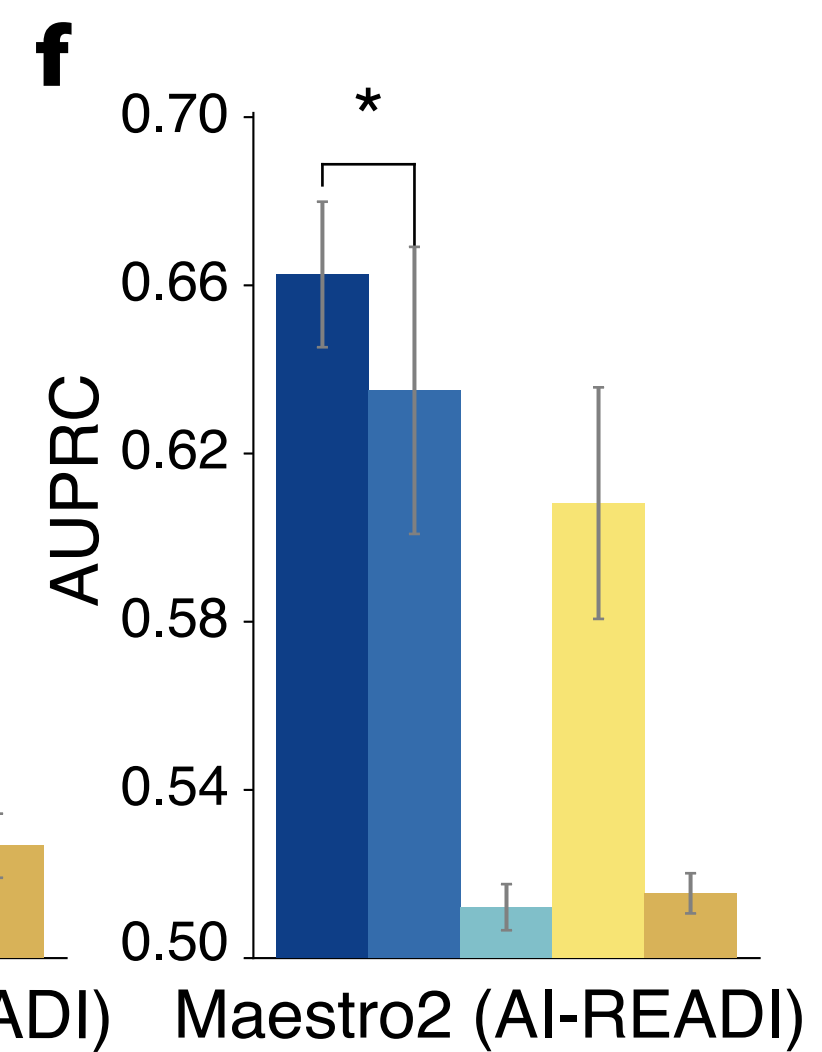
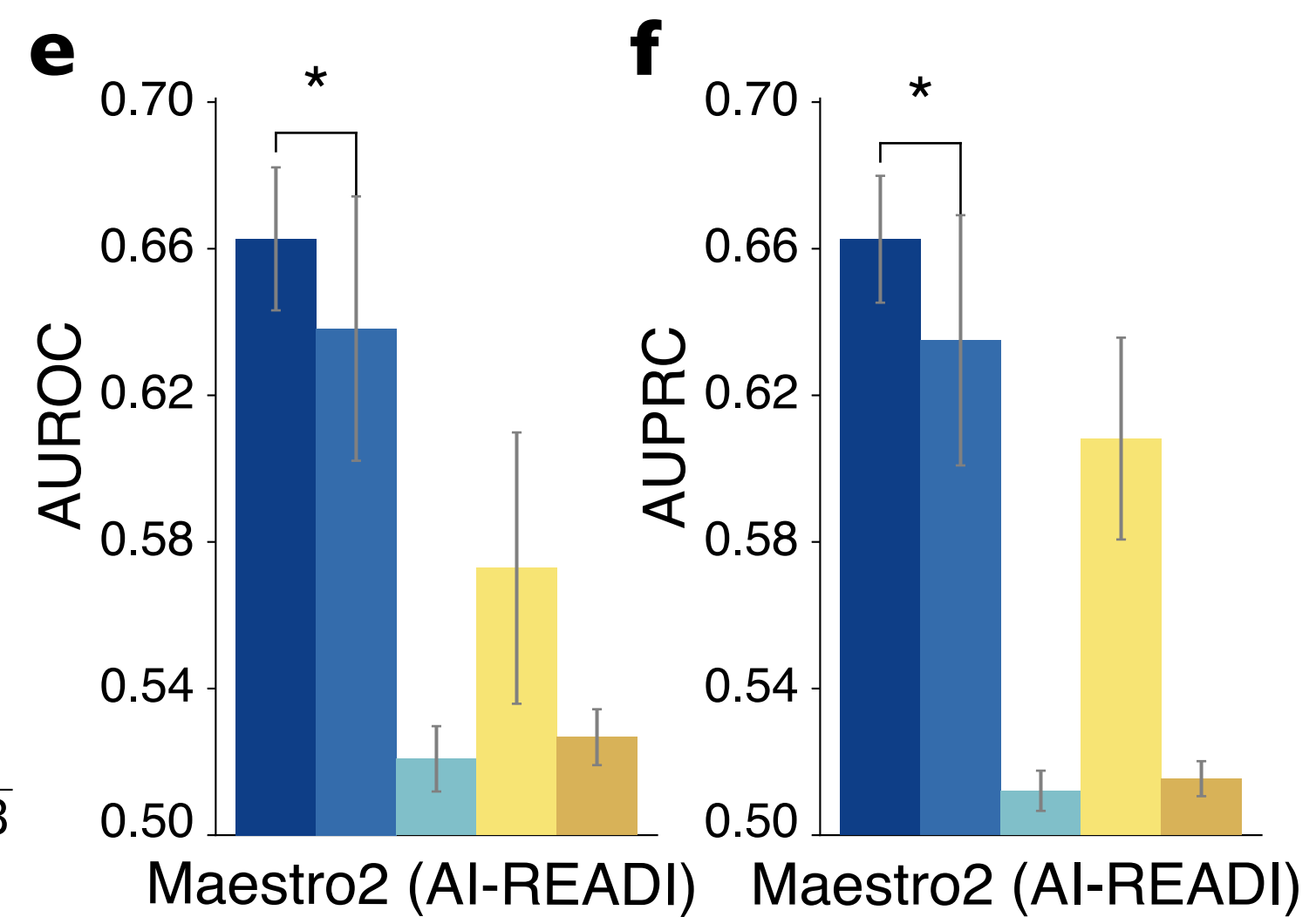
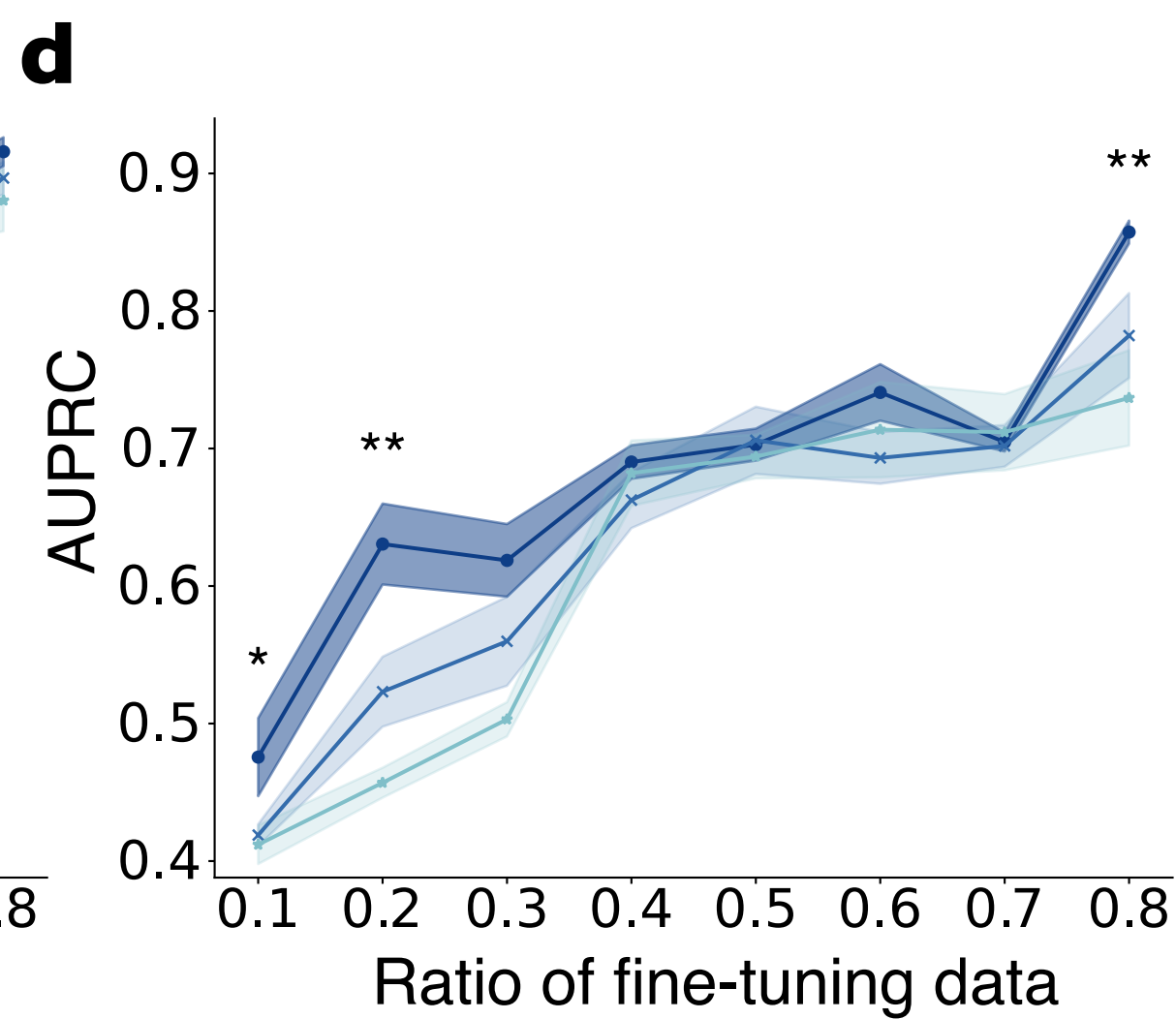
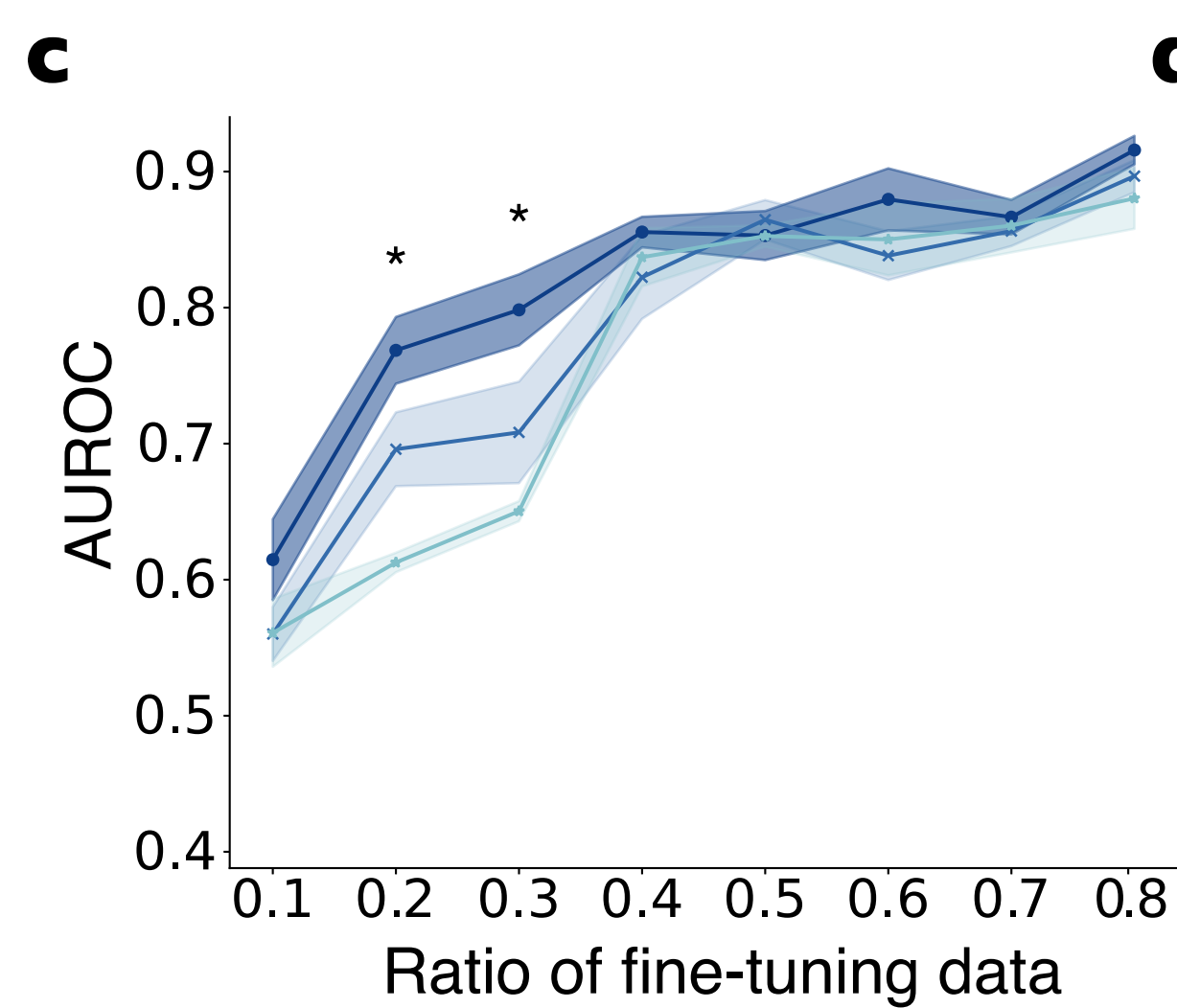
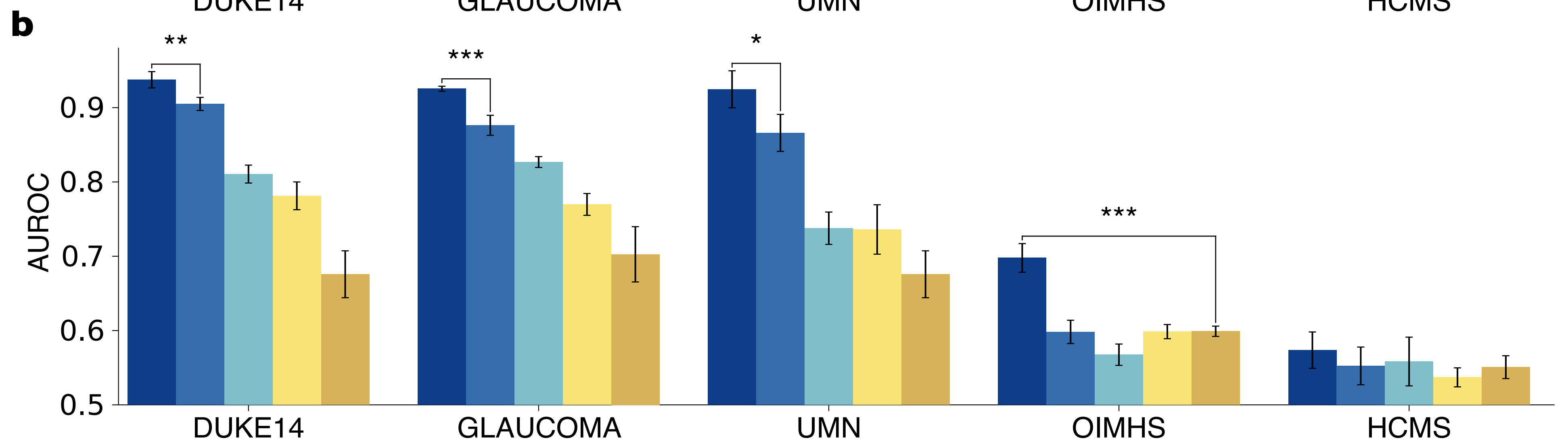
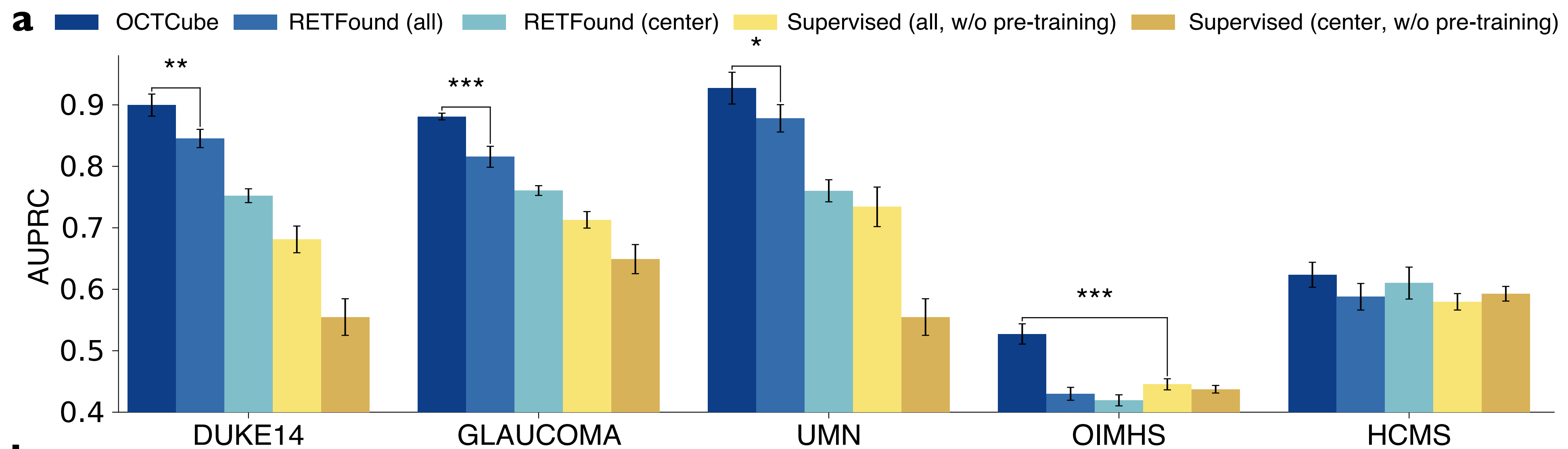
- Neural Inf. Process. Syst.* 4765–4774 (2017).
59. Chefer, H., Gur, S. & Wolf, L. Transformer Interpretability Beyond Attention Visualization. in *2021 IEEE/CVF Conference on Computer Vision and Pattern Recognition (CVPR)* (IEEE, 2021). doi:10.1109/cvpr46437.2021.00084.
 60. Zhao, Q., Liu, Z., Adeli, E. & Pohl, K. M. Longitudinal self-supervised learning. *Med. Image Anal.* **71**, 102051 (2021).
 61. Liu, Z. *et al.* *ForeSeer: Product Aspect Forecasting Using Temporal Graph Embedding*. (2023).
 62. Srivastava, N., Hinton, G. E., Krizhevsky, A., Sutskever, I. & Salakhutdinov, R. Dropout: a simple way to prevent neural networks from overfitting. *J. Mach. Learn. Res.* **15**, 1929–1958 (2014).
 63. Hendrycks, D. & Gimpel, K. Gaussian Error Linear Units (GELUs). *arXiv [cs.LG]* (2016).
 64. Chattopadhyay, A., Sarkar, A., Howlader, P. & Balasubramanian, V. N. Grad-CAM++: Generalized gradient-based visual explanations for deep convolutional networks. in *2018 IEEE Winter Conference on Applications of Computer Vision (WACV)* (IEEE, 2018). doi:10.1109/wacv.2018.00097.
 65. Gildenblat, J. & Contributors, D. PyTorch library for CAM methods. Preprint at <https://github.com/jacobgil/pytorch-grad-cam> (2021).
 66. Rashno, A. *et al.* Fully-automated segmentation of fluid regions in exudative age-related macular degeneration subjects: Kernel graph cut in neutrosophic domain. *PLoS One* **12**, e0186949 (2017).
 67. Srinivasan, P. P. *et al.* Fully automated detection of diabetic macular edema and dry age-related macular degeneration from optical coherence tomography images. *Biomed. Opt.*

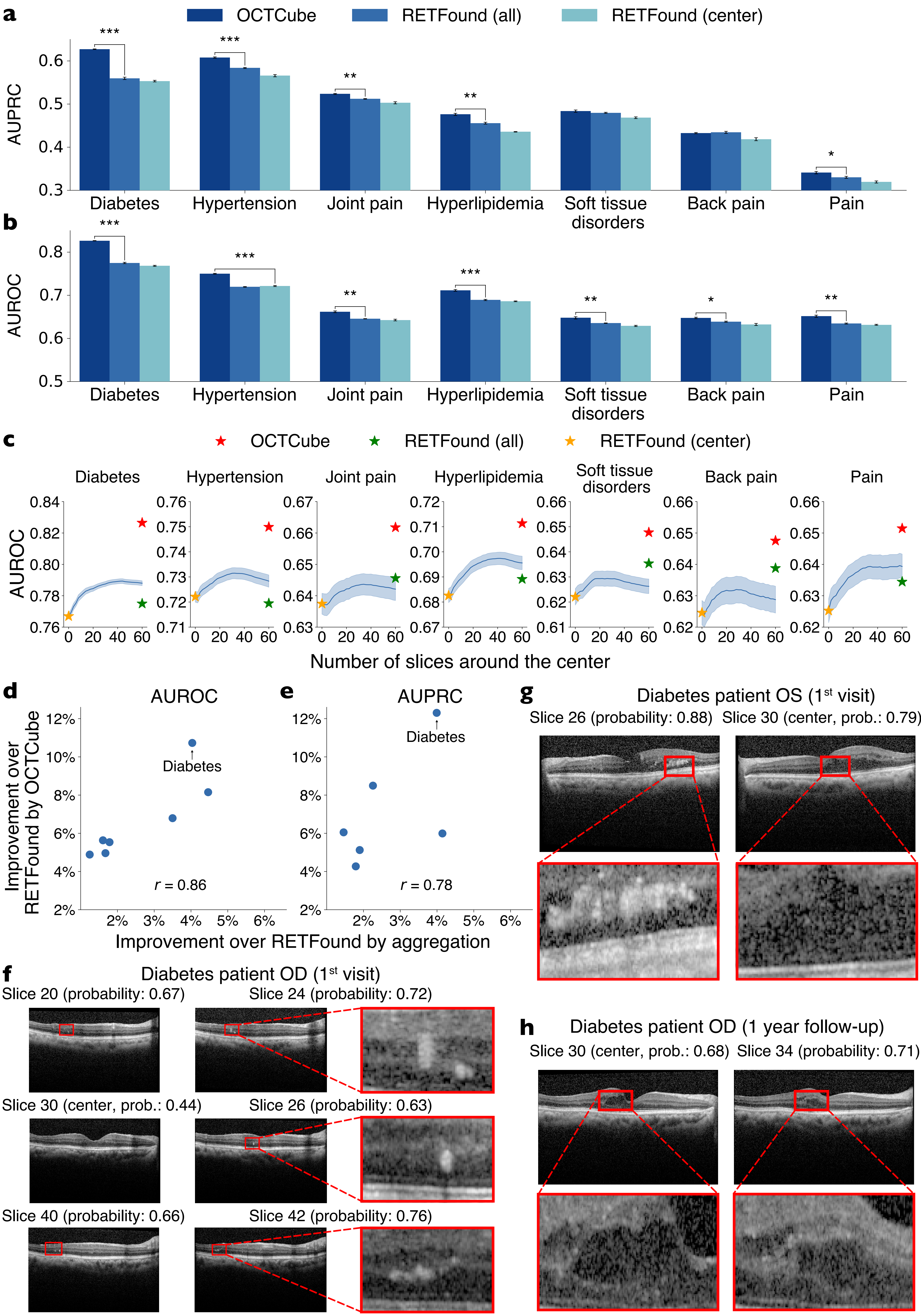
Express **5**, 3568–3577 (2014).

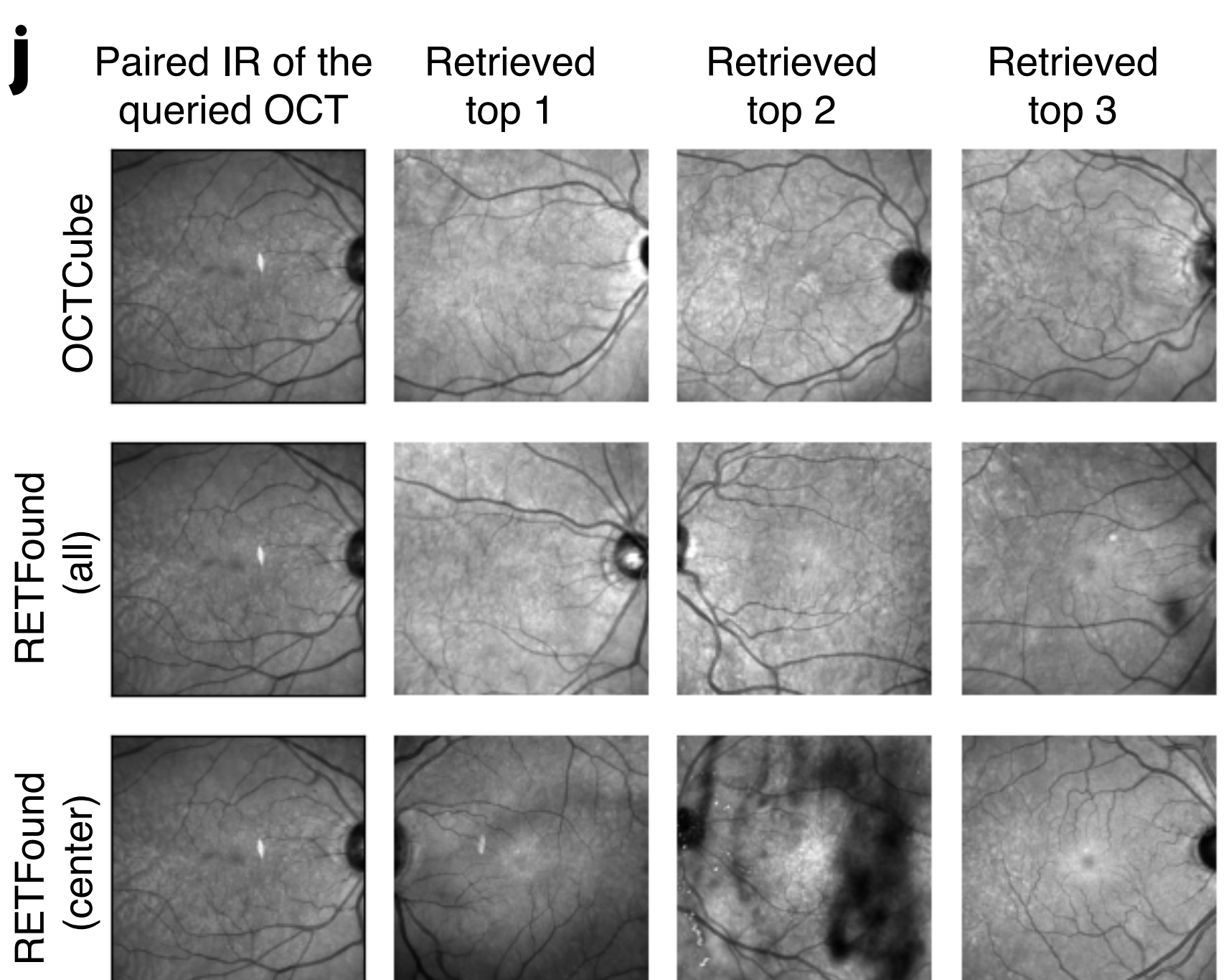
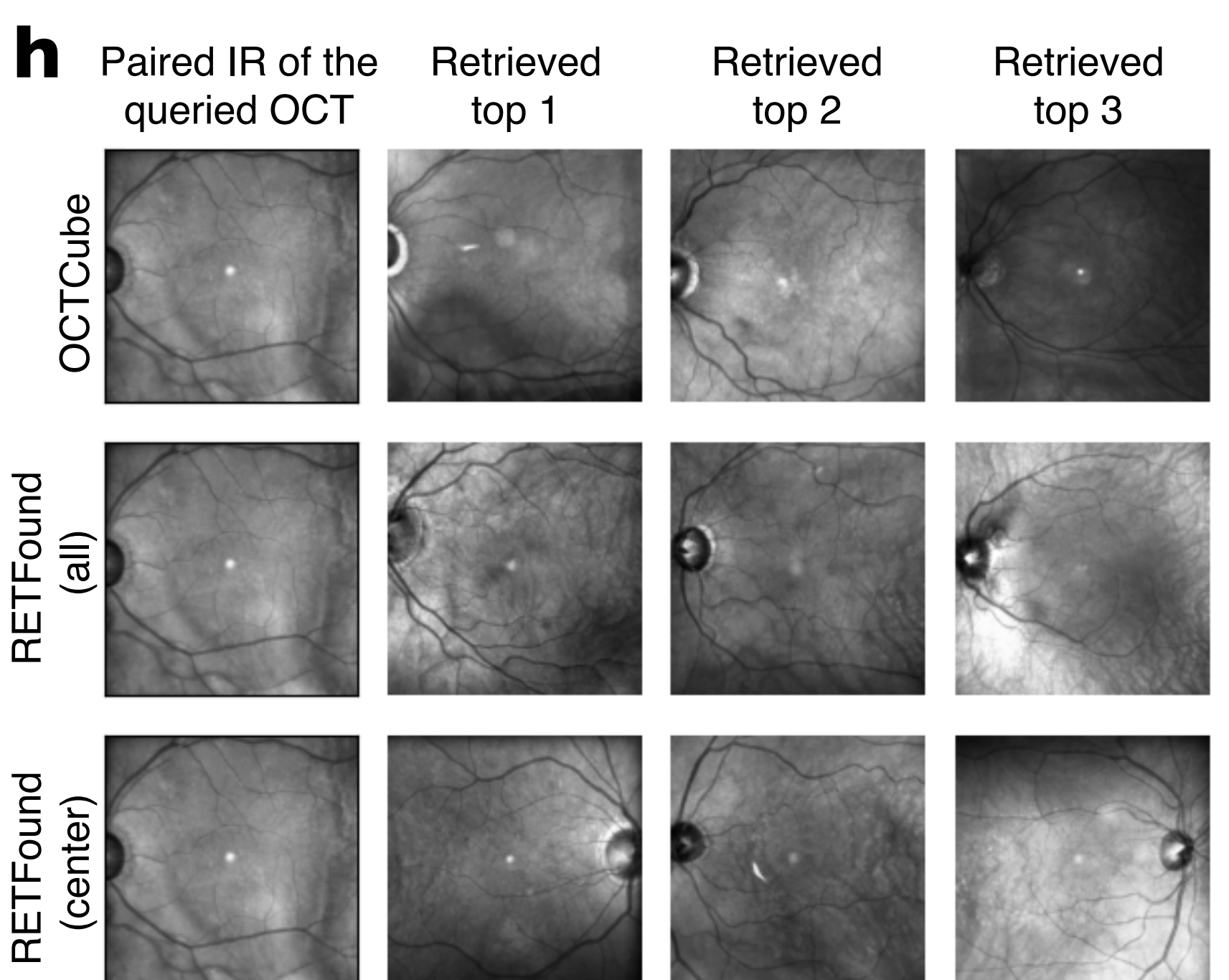
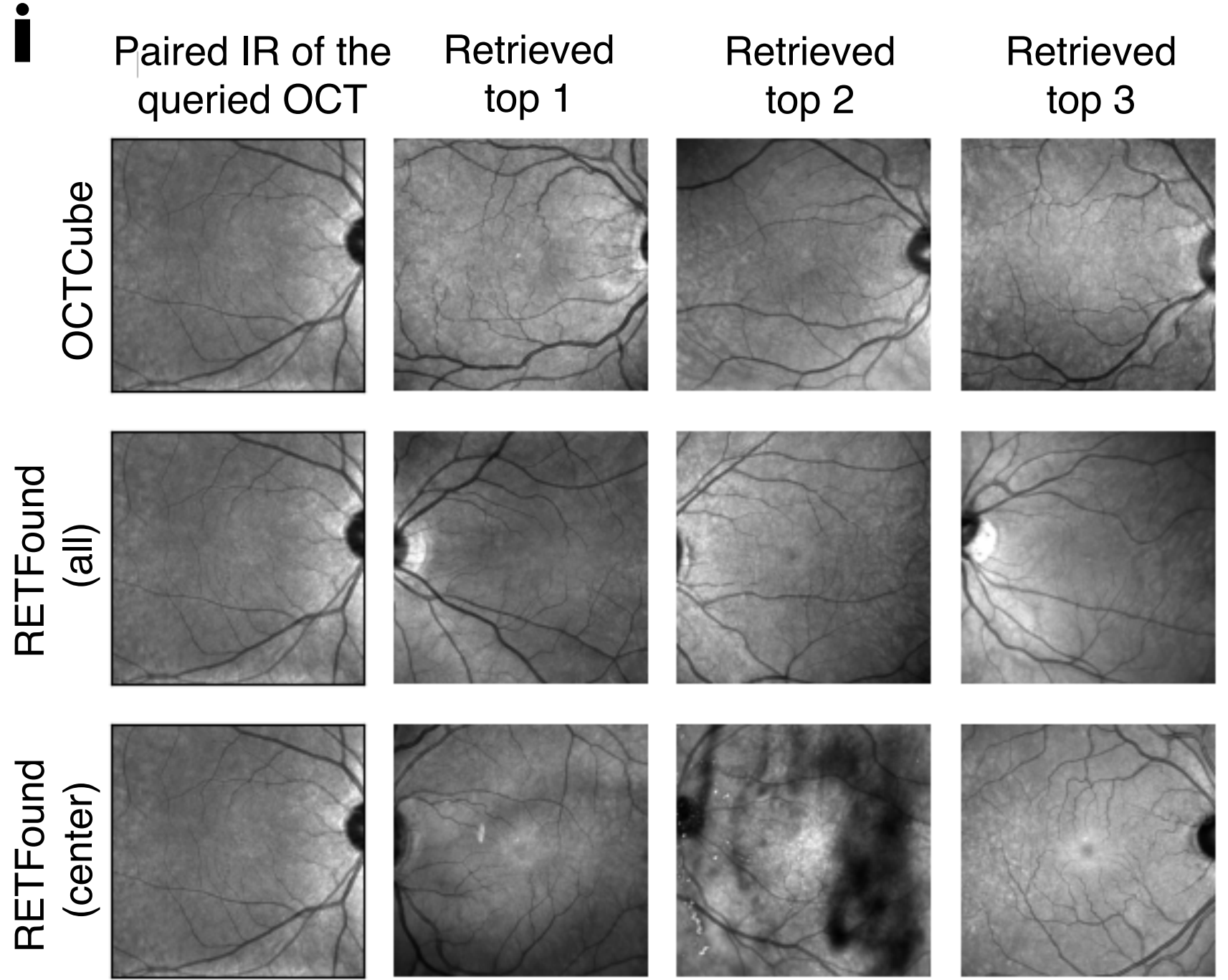
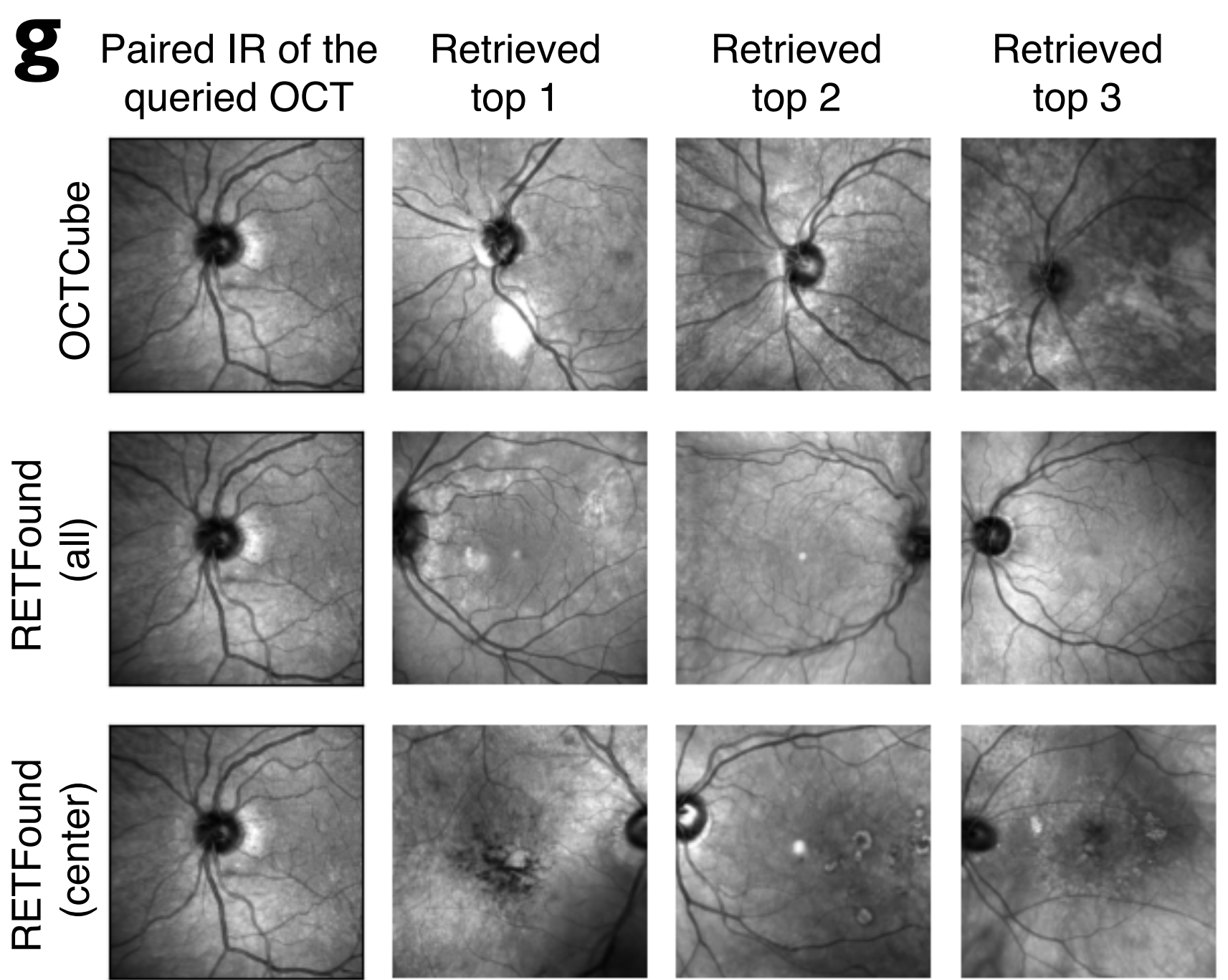
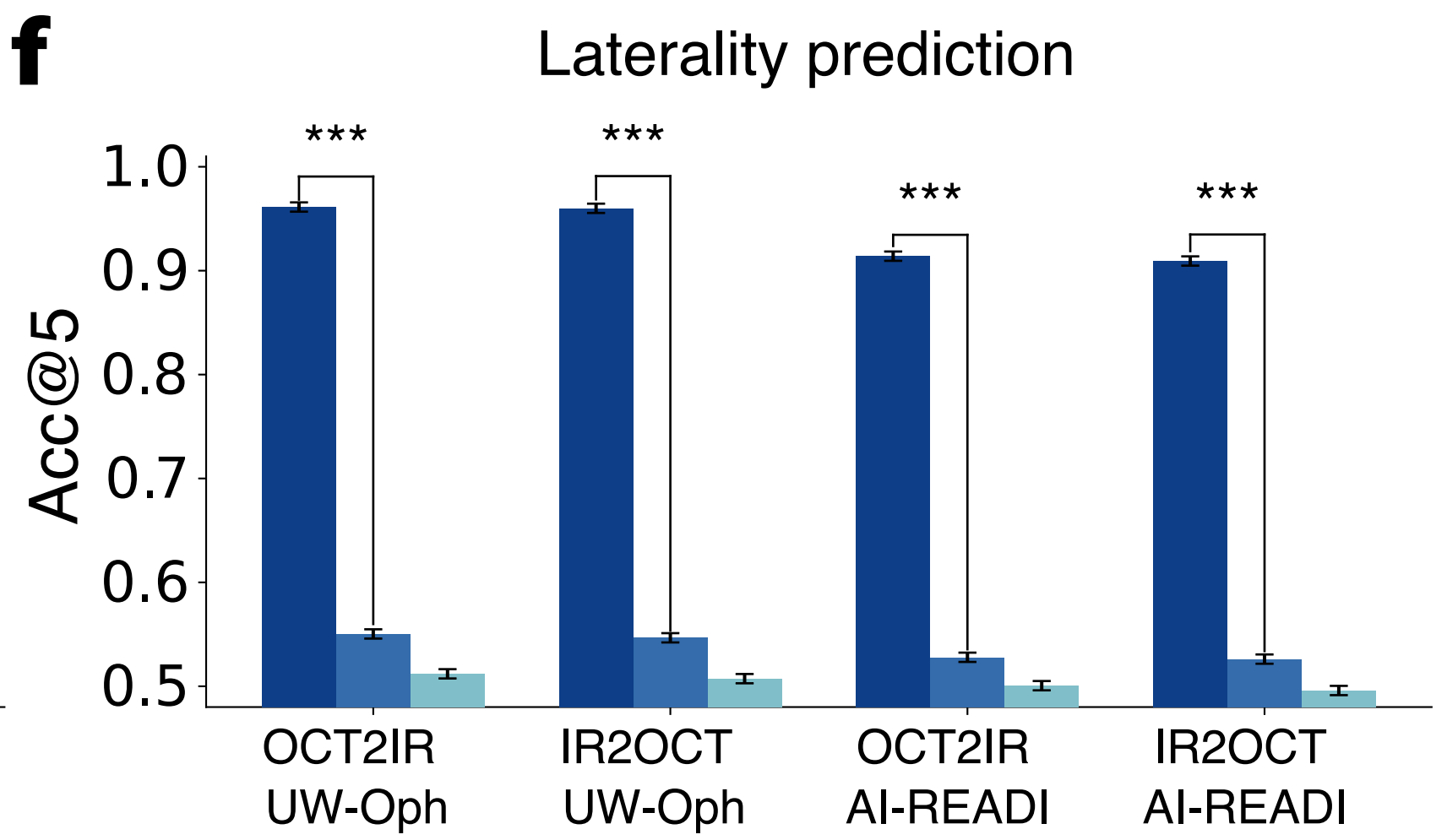
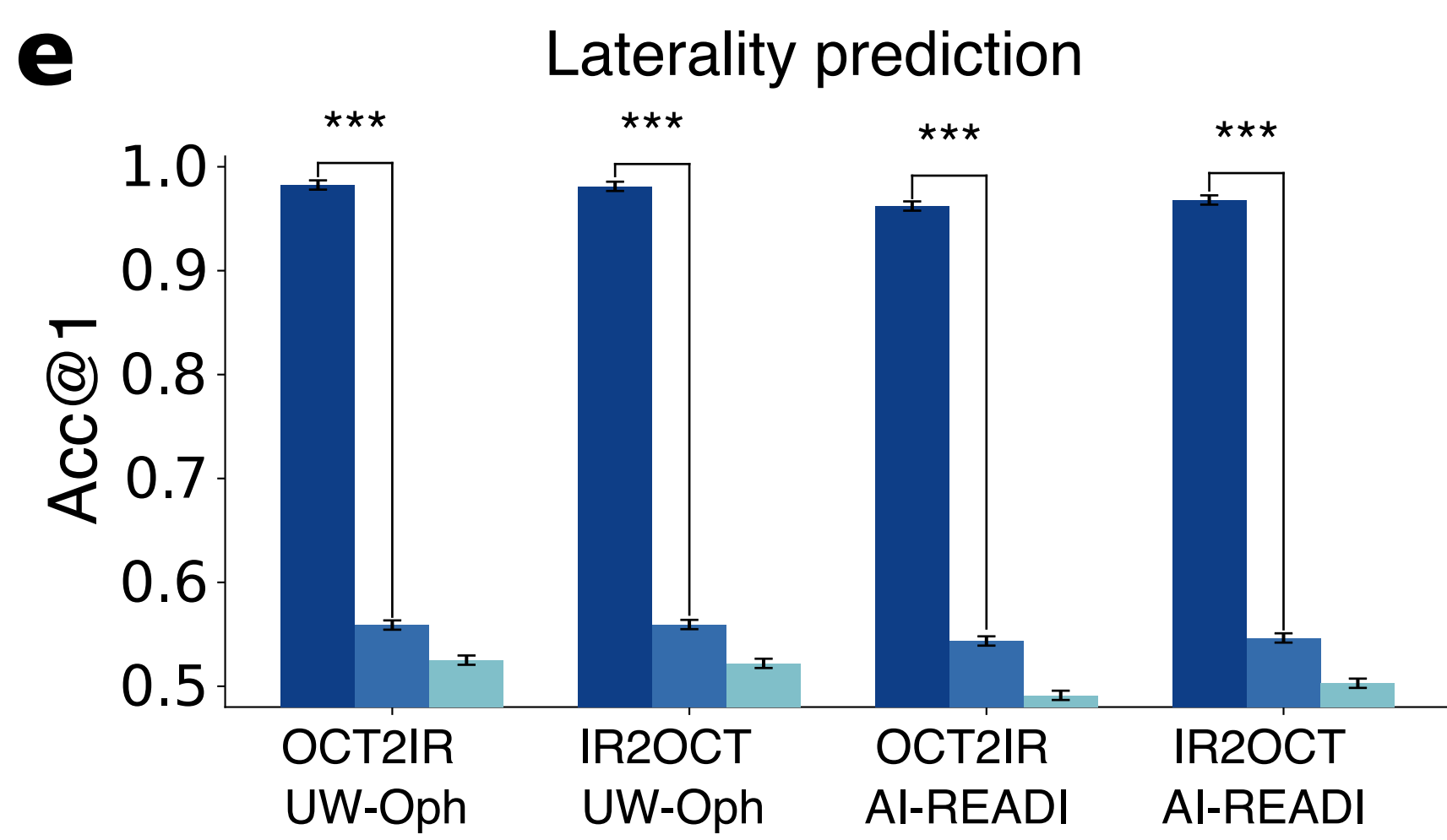
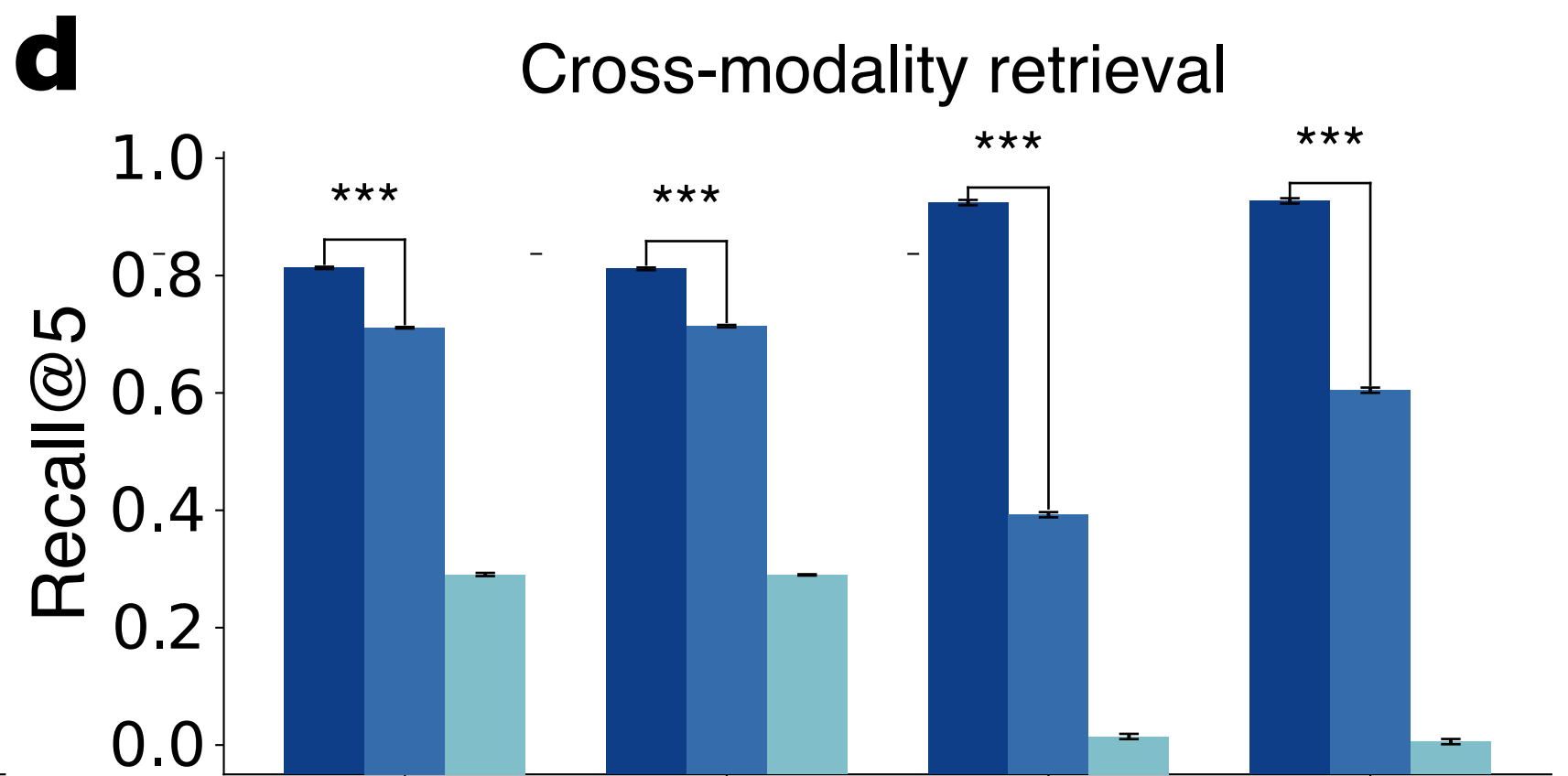
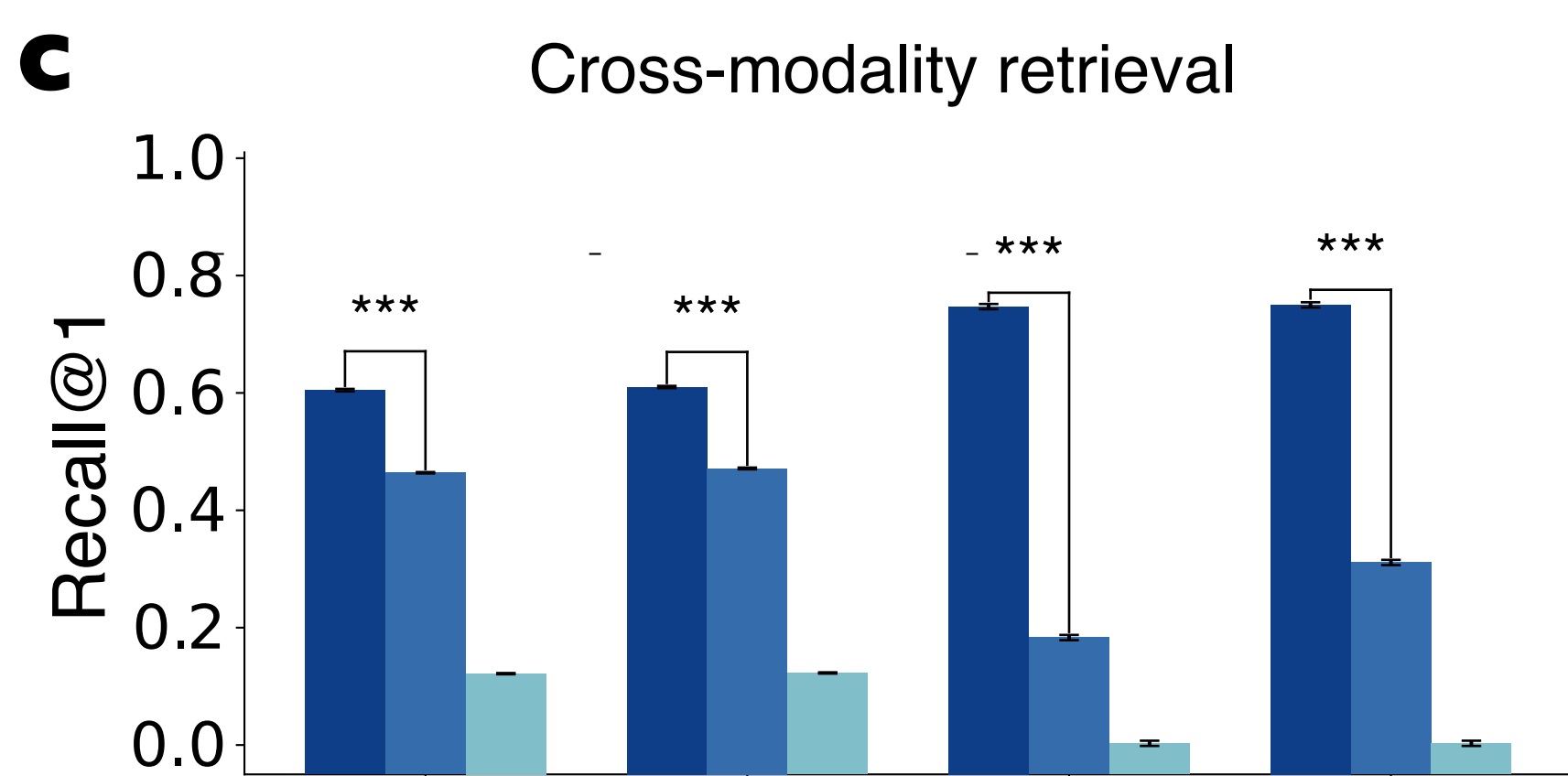
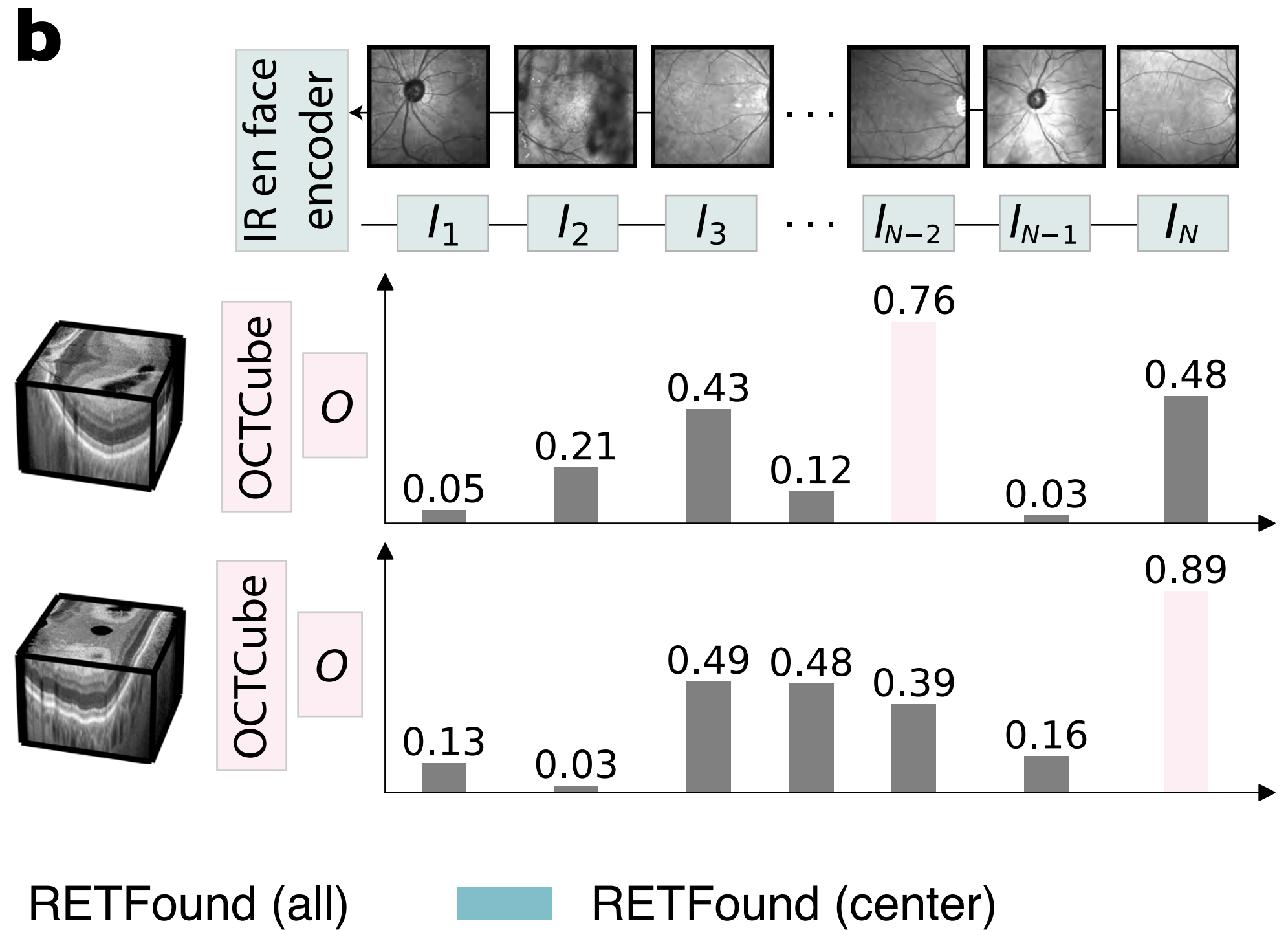
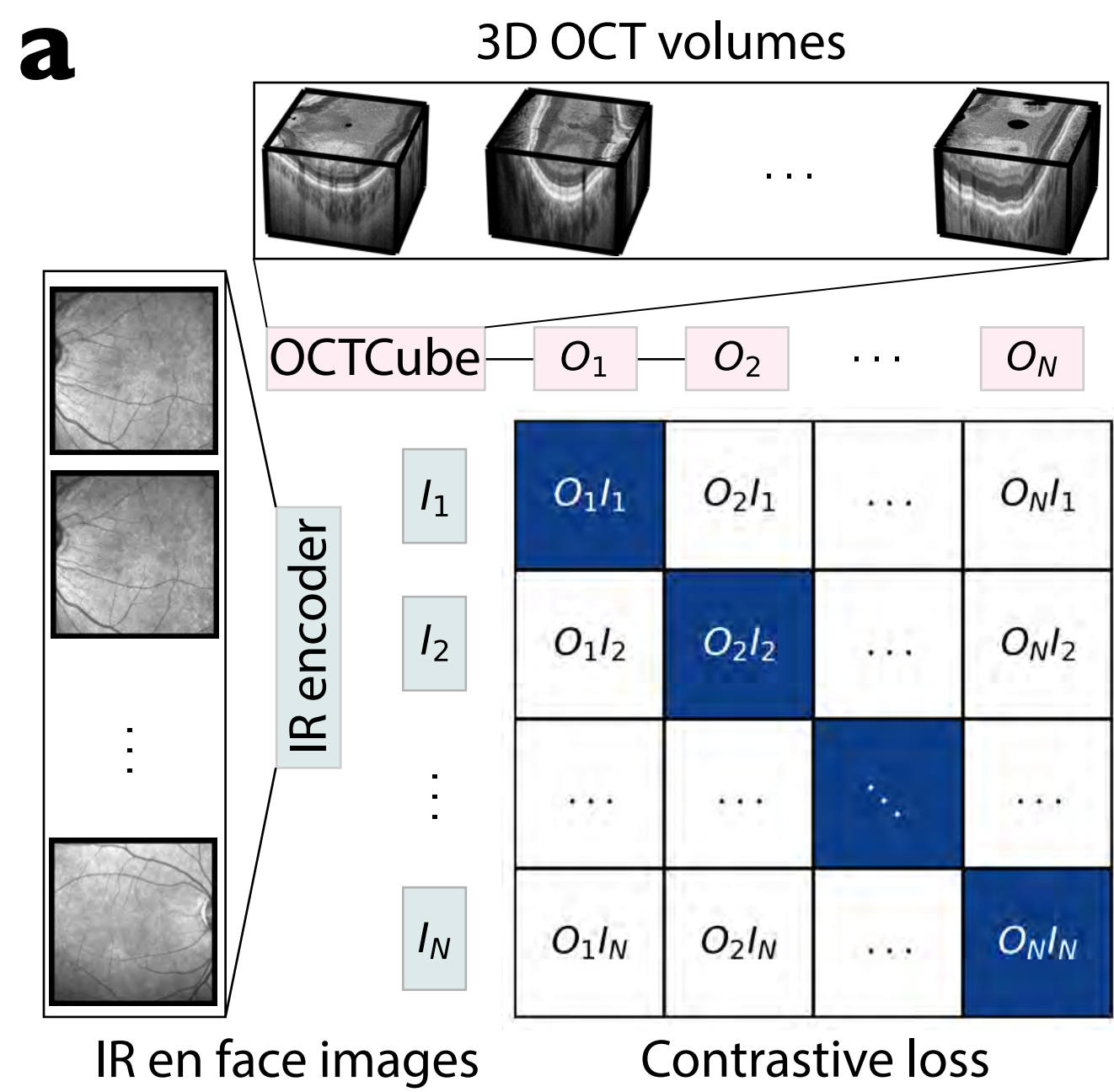
68. He, Y. *et al.* Retinal layer parcellation of optical coherence tomography images: Data resource for multiple sclerosis and healthy controls. *Data Brief* **22**, 601–604 (2019).
69. Otsu, N. A threshold selection method from gray-level histograms. *IEEE Trans. Syst. Man Cybern.* **9**, 62–66 (1979).
70. Radford, A. *et al.* Learning Transferable Visual Models From Natural Language Supervision. in *Proceedings of the 38th International Conference on Machine Learning* (eds. Meila, M. & Zhang, T.) vol. 139 8748–8763 (PMLR, 18–24 Jul 2021).
71. van den Oord, A., Li, Y. & Vinyals, O. Representation learning with Contrastive Predictive Coding. *ArXiv* **abs/1807.03748**, (2018).
72. Creators Ilharco, Gabriel Wortsman, Mitchell Carlini, Nicholas Taori, Rohan Dave, Achal Shankar, Vaishaal Namkoong, Hongseok Miller, John Hajishirzi, Hannaneh Farhadi, Ali Schmidt, Ludwig. *OpenCLIP*. doi:10.5281/zenodo.5143773.
73. Paszke, A. *et al.* PyTorch: An imperative style, high-performance deep learning library. *Adv. Neural Inf. Process. Syst.* **abs/1912.01703**, (2019).
74. Zhang, S. *et al.* BiomedCLIP: a multimodal biomedical foundation model pretrained from fifteen million scientific image-text pairs. *arXiv preprint arXiv:2303.00915* (2023).

a OCTCube RETFound (all) RETFound (center) Supervised (all, w/o pre-training) Supervised (center, w/o pre-training)









Supplementary File for OCTCube: A 3D foundation model for optical coherence tomography that improves cross-dataset, cross-disease, cross-device and cross-modality analysis.

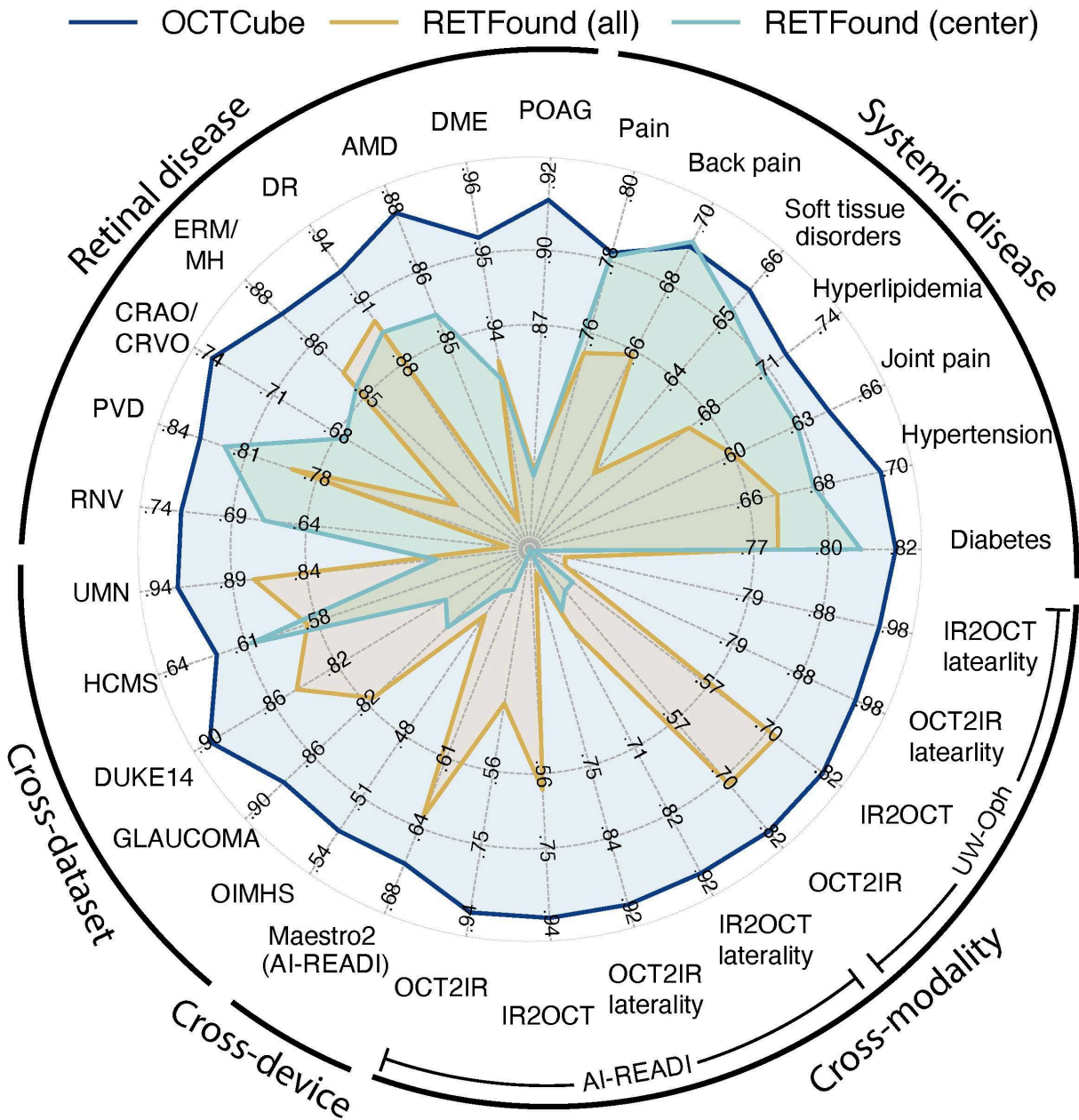
Zixuan Liu¹, Hanwen Xu¹, Addie Woicik¹, Linda G. Shapiro¹, Marian Blazes^{2,3}, Yue Wu^{2,3}, Cecilia S. Lee^{2,3}, Aaron Y. Lee^{2,3}[#], Sheng Wang¹[#]

¹Paul G. Allen School of Computer Science and Engineering, University of Washington, Seattle, WA

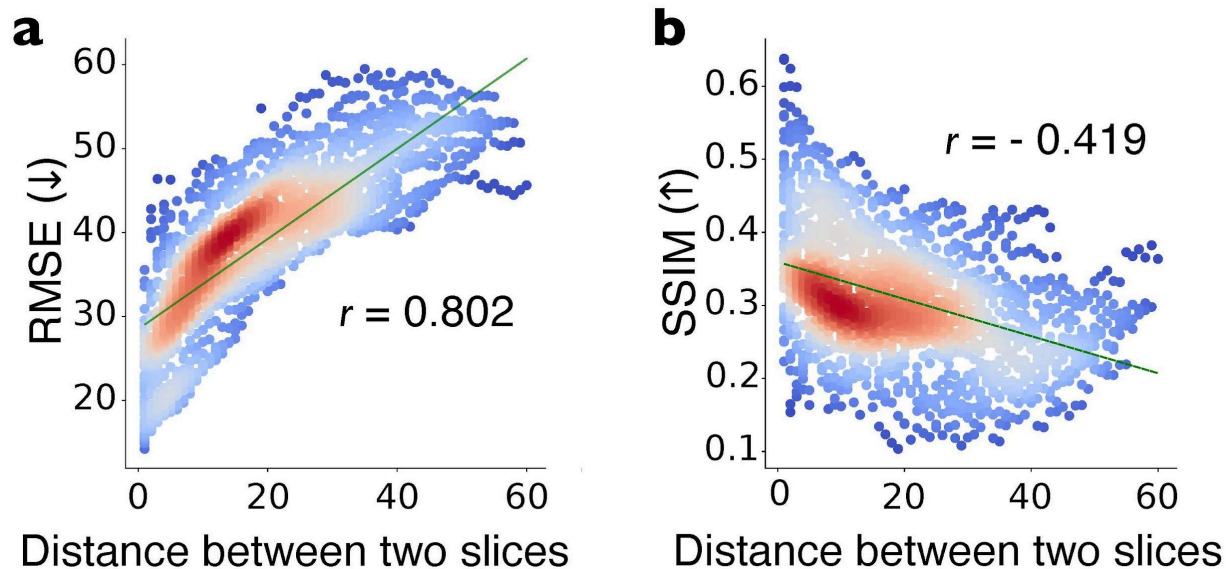
²Department of Ophthalmology, University of Washington, Seattle, WA, USA

³Roger and Angie Karalis Johnson Retina Center, University of Washington, Seattle, WA, USA

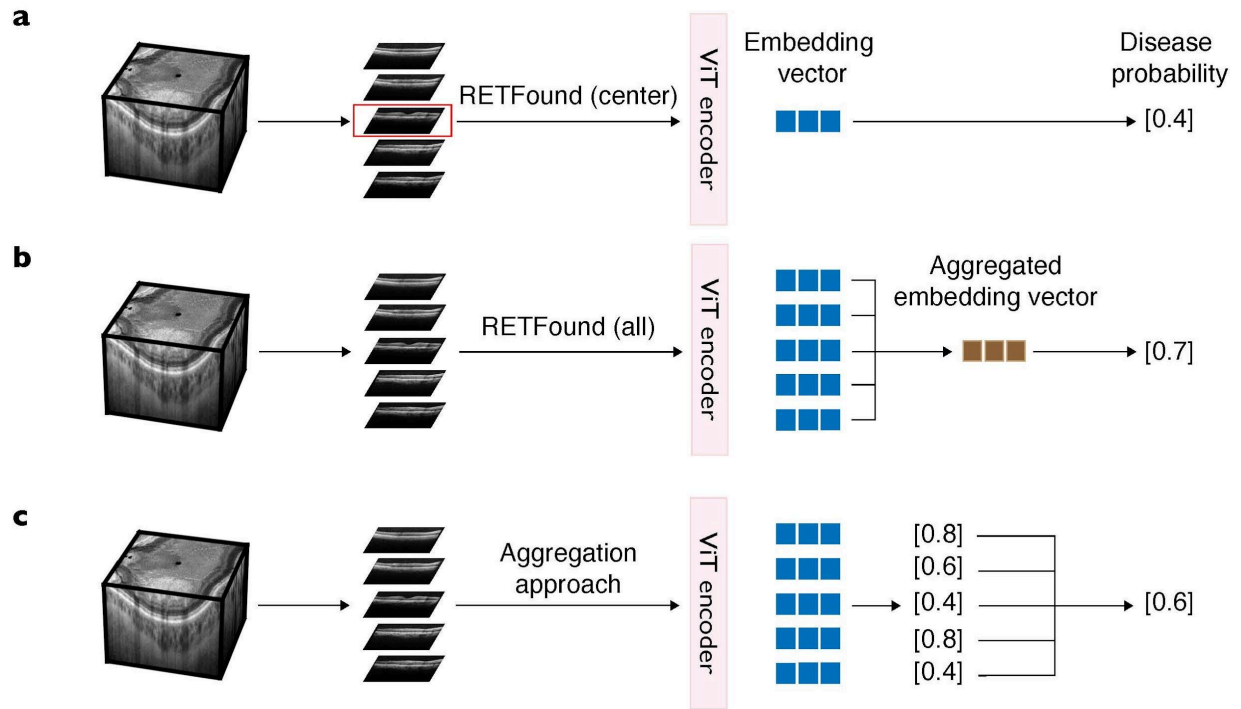
[#]Email: leeay@uw.edu , swang@cs.washington.edu



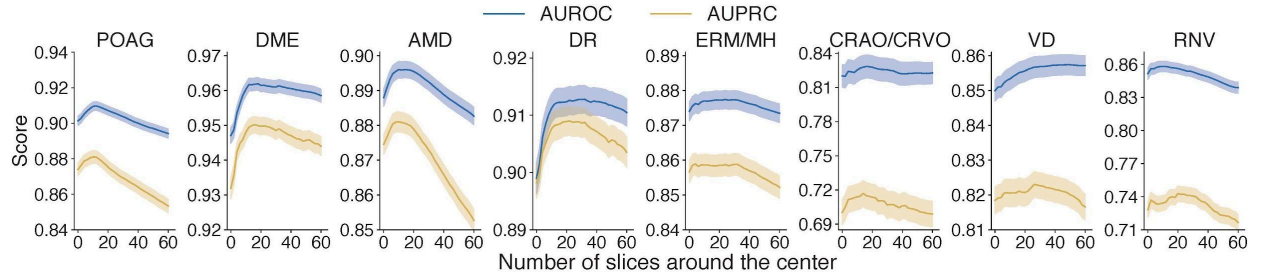
Supplementary Fig. 1 Radar plot comparing the performance of OCTCube and competing methods on 29 tasks, including eight retinal disease prediction tasks in the inductive learning setting, five retinal disease prediction tasks in the inductive learning setting, seven systemic disease prediction tasks, eight cross-modality retrieval tasks and one cross-device prediction task. Recall@5 is used as the metric for the cross-modal retrieval tasks, Acc@5 is used as the metric for the cross-modal laterality prediction tasks, while AUPRC is used as the metric for the other tasks. UW-Oph is the abbreviation for UW Ophthalmology dataset.



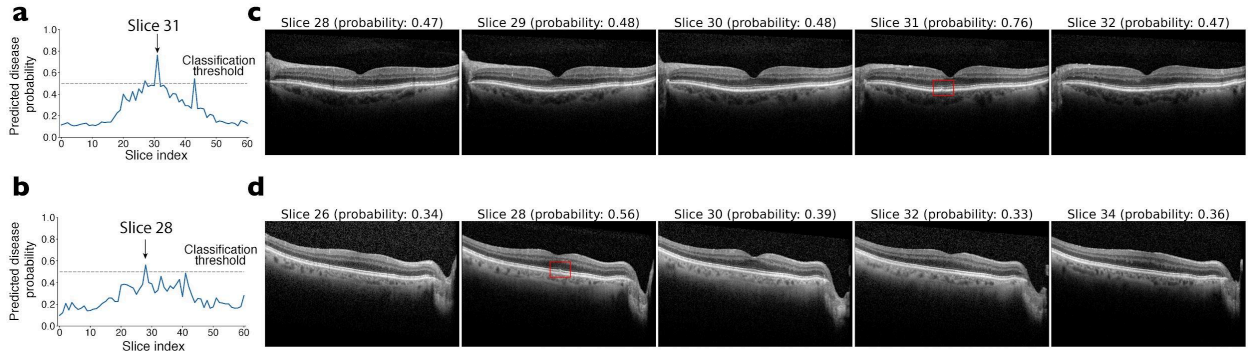
Supplementary Fig. 2 a-b, Scatter plots comparing the similarity of two slices in an OCT volume in terms of RMSE (a) and SSIM (b). X-axis indicates the distance between two slices in the same volume. r denotes Pearson correlation coefficient.



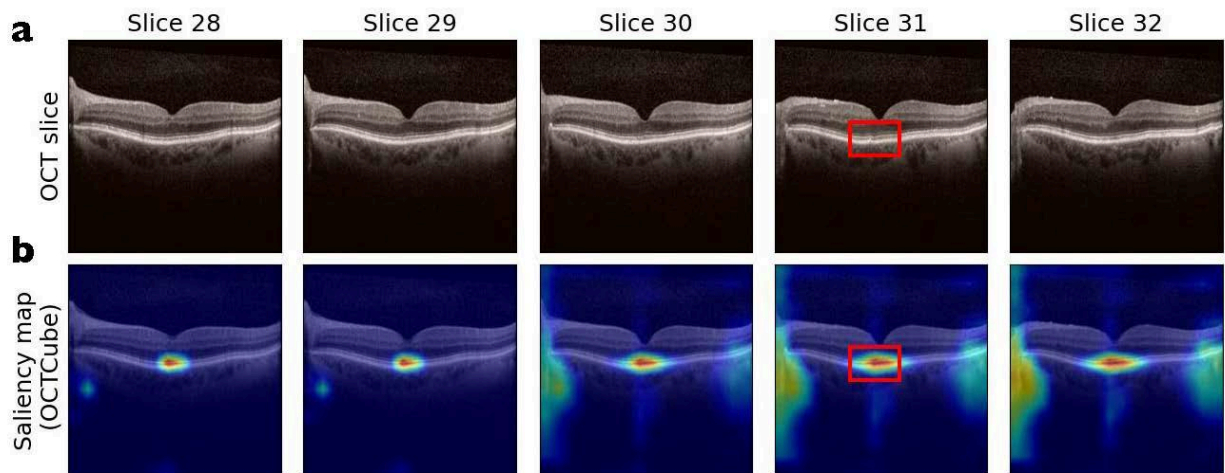
Supplementary Fig. 3 Illustration of various competing methods. **a**, RETFound (center) extracts the center slice and generates predictions based on it. **b**, RETFound (all) takes all slices as input, extracts embeddings for each slice, averages all embeddings, and gets the final prediction score using neural networks. **c**, The aggregation approach first generates the prediction score for every slice using RETFound (center), and then averages the prediction scores to get the final prediction score.



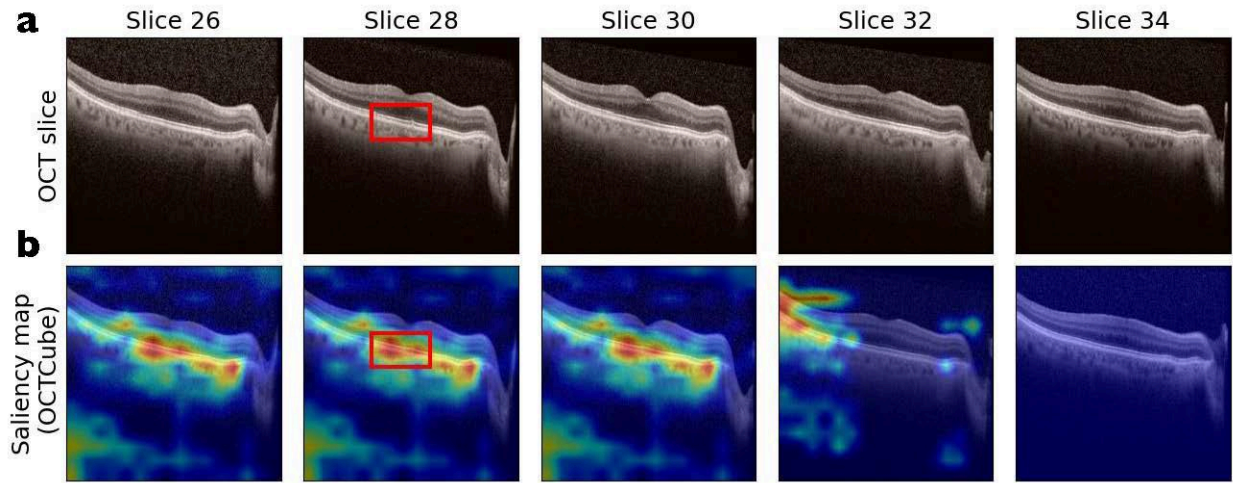
Supplementary Fig. 4 Plots showing the AUROC and AUPRC of an aggregation approach that averages the prediction probabilities using each of the k slices around the center slices on eight retinal diseases, where k is shown in the x-axis. The prediction probability for each slice is derived using RETFound. POAG, DME, AMD, ERM/MH, DR, CRAO/CRVO, VD, RNV denote primary open-angle glaucoma, diabetic macular edema, age-related macular degeneration, epiretinal membrane or macular hole, diabetic retinopathy without macular edema, central retinal vein / artery occlusion, vitreous degeneration, and retinal neovascularization respectively.



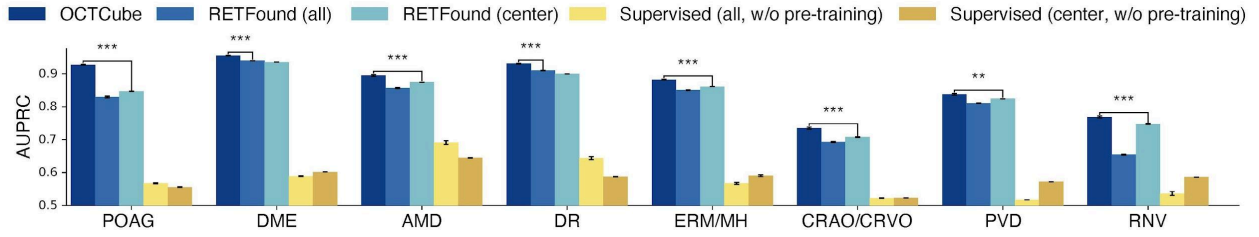
Supplementary Fig. 5 a,b, Plots showing the prediction probabilities of age-related macular degeneration (AMD) by using each slice as the input for RETFound on two AMD patients. While the center slice (slice 30) incorrectly predicts AMD as negative, there exist other slices near the center slice that correctly predict AMD as positive. Slice 31 for the first patient (**a**) and slice 28 for the second patient (**b**) achieve the highest prediction probability, suggesting the possibility to improve the prediction performance by considering the 3D structure. **c,d,** Visualization of the OCT slices around the center slice (slice 30) and the corresponding prediction probabilities of the AMD patient (**c** for patient 1 and **d** for patient 2). Red boxes highlight the small drusen that occurs at the slice 31 of patient 1 and the slice 28 of patient 2, indicating signals for AMD.



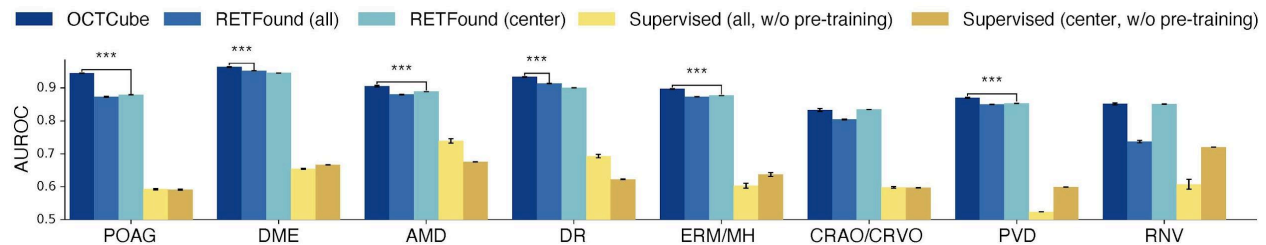
Supplementary Fig. 6 a-b, Visualization of multiple slices across the slow-scan dimension from the OCT volume studied in **Fig. 1c** with the OCT slices (**a**) and saliency maps based on the prediction of OCTCube (**b**). The drusen area occurs in slice 31, as also indicated by the generated saliency maps. Images are resized to (256, 256) for the purpose of visualization. Red pixels in (**b**) indicate higher importance, while blue pixels indicate lower importance. The red bounding boxes are manually drawn based on the saliency map.



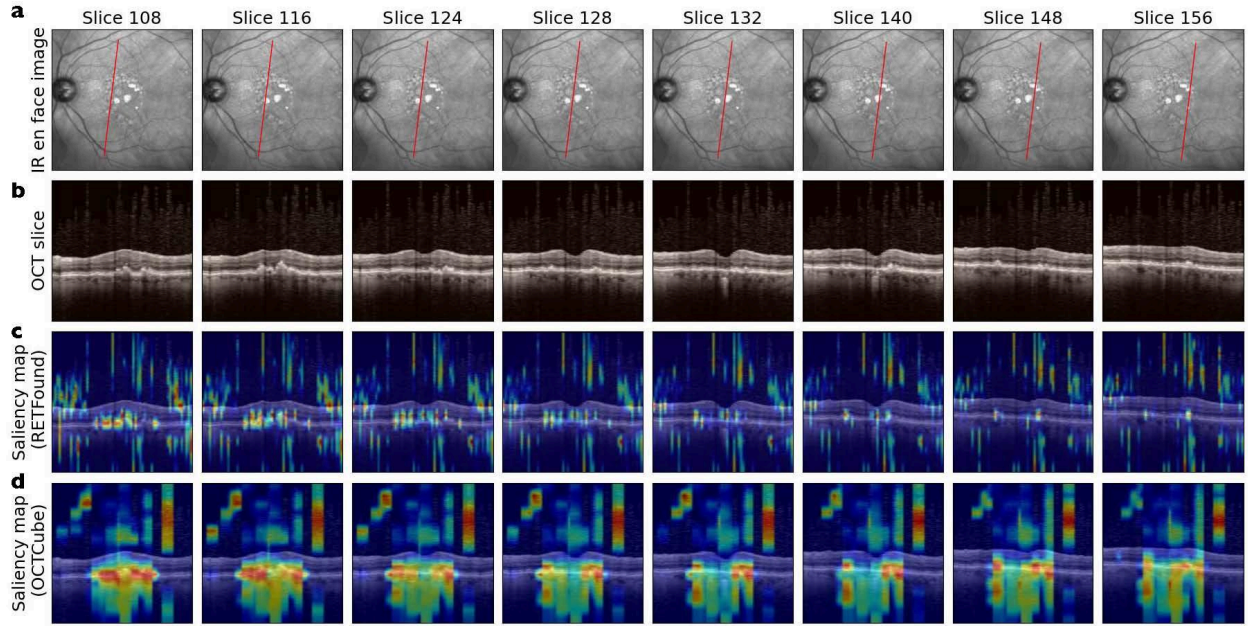
Supplementary Fig. 7 a-b, Visualization of multiple slices across the slow-scan dimension from the OCT volume studied in **Fig. 1d** with the OCT slices (**a**) and saliency maps based on the prediction of OCTCube (**b**). The drusen area occurs in slice 28, as also indicated by the generated saliency maps. Images are resized to (256, 256) for the purpose of visualization. Red pixels in (**b**) indicate higher importance, while blue pixels indicate lower importance. The red bounding boxes are manually drawn based on the saliency map.



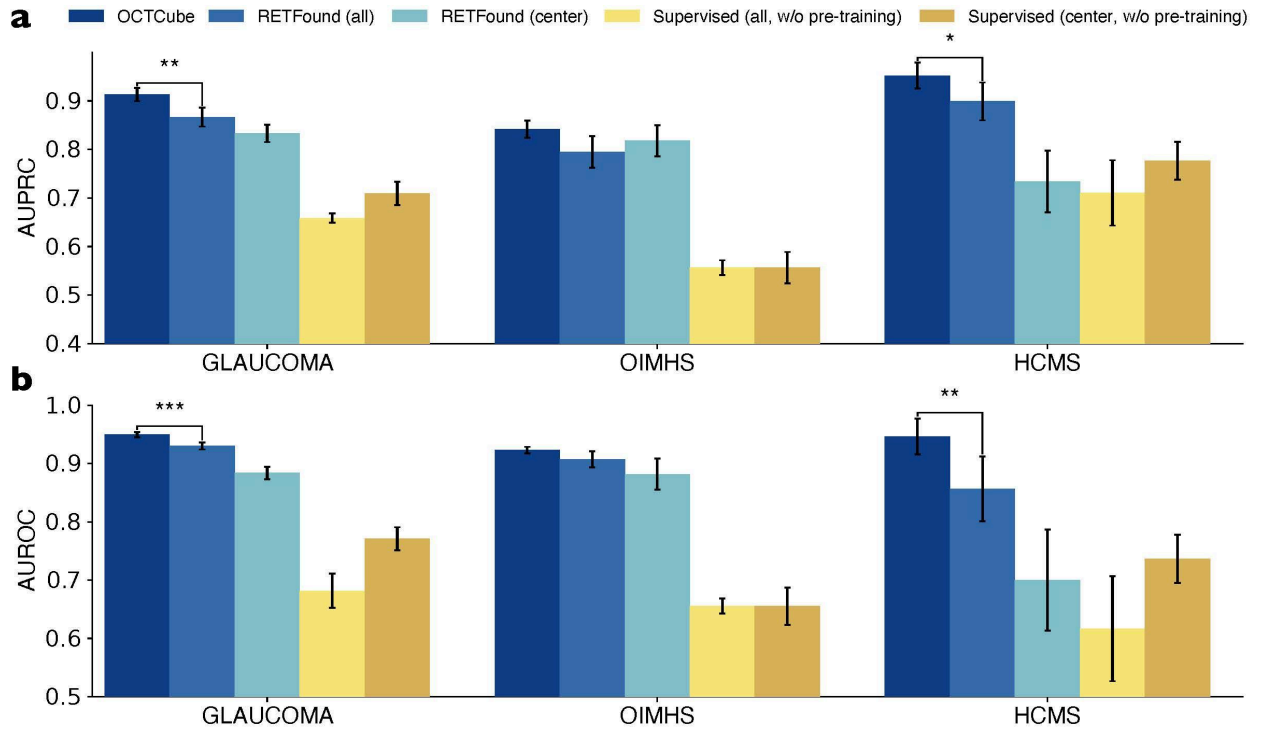
Supplementary Fig. 8 Barplots comparing OCTCube and competing methods on disease classification of 8 retinal diseases on UW Ophthalmology dataset in terms of AUPRC. Inductive learning setting is used to ensure that test OCT volumes are not seen by OCTCube in the pre-training stage. The train:validation:test split is set to be 60%:20%:20%. POAG, DME, AMD, ERM/MH, DR, CRAO/CRVO, PVD, RNV denote primary open-angle glaucoma, diabetic macular edema, age-related macular degeneration, epiretinal membrane or macular hole, diabetic retinopathy without macular edema, central retinal vein / artery occlusion, posterior vitreous detachment, and retinal neovascularization respectively. Supervised approaches do not have a pre-training stage. RETFound (all) and Supervised (all) average the embeddings of all slices within a 3D volume. * indicates the significance level at which OCTCube outperforms the best-competing method, with paired t-test p-value $< 5 \times 10^{-2}$ for *, p-value $< 1 \times 10^{-2}$ for **, p-value $< 1 \times 10^{-3}$ for ***.



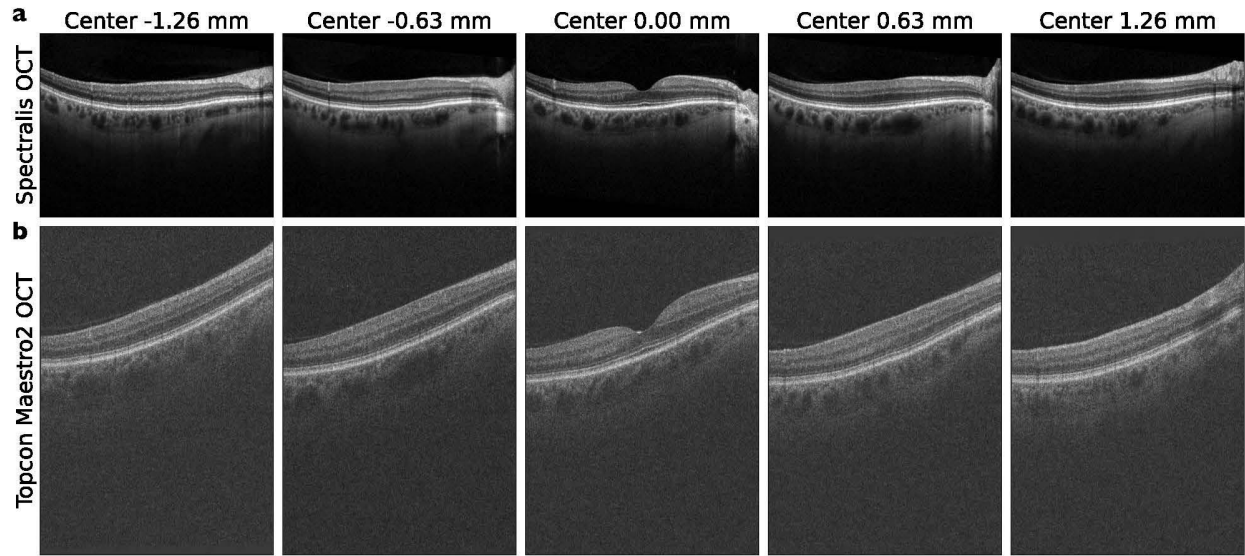
Supplementary Fig. 9 Barplots comparing OCTCube and competing methods on disease classification of 8 retinal diseases on UW Ophthalmology dataset in terms of AUROC. Inductive learning setting is used to ensure that test OCT volumes are not seen by OCTCube in the pre-training stage. The train:validation:test split is set to be 60%:20%:20%. POAG, DME, AMD, PM, DR, CRAO/CRVO, VD, RNV denote primary open-angle glaucoma, diabetic macular edema, age-related macular degeneration, epiretinal membrane or macular hole, diabetic retinopathy without macular edema, central retinal vein / artery occlusion, vitreous degeneration, and retinal neovascularization respectively. Supervised approaches do not have a pre-training stage. RETFound (all) and Supervised (all) average the embeddings of all slices within a 3D volume. * indicates the significance level at which OCTCube outperforms the best-competing method, with paired t-test p-value $< 5 \times 10^{-2}$ for *, p-value $< 1 \times 10^{-2}$ for **, p-value $< 1 \times 10^{-3}$ for ***.



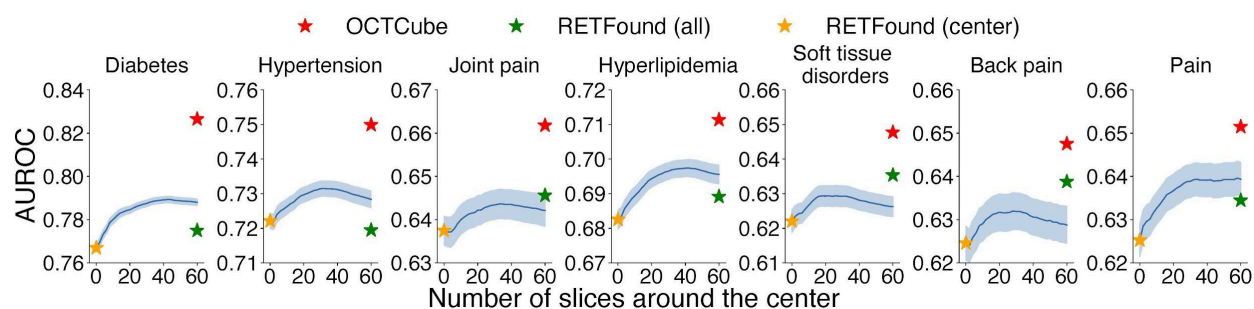
Supplementary Fig. 10 a-d, Visualization of multiple slices across the slow-scan dimension from a single OCT volume with the sampling location (a) in the corresponding IR en face image, OCT slices (b), saliency maps based on the prediction of RETFound (center) (c), and saliency maps based on the prediction of OCTCube (d). OCTCube provides a more coherent saliency map across slices in the diseased area, indicating the effectiveness of the 3D modeling. The aspect ratio is adjusted from (61, 496) to (256, 256) for the purpose of visualization. Red in (c,d) indicates higher saliency. Red lines in (a) are drawn with the consideration of pixel spacing of sampled OCT slices.



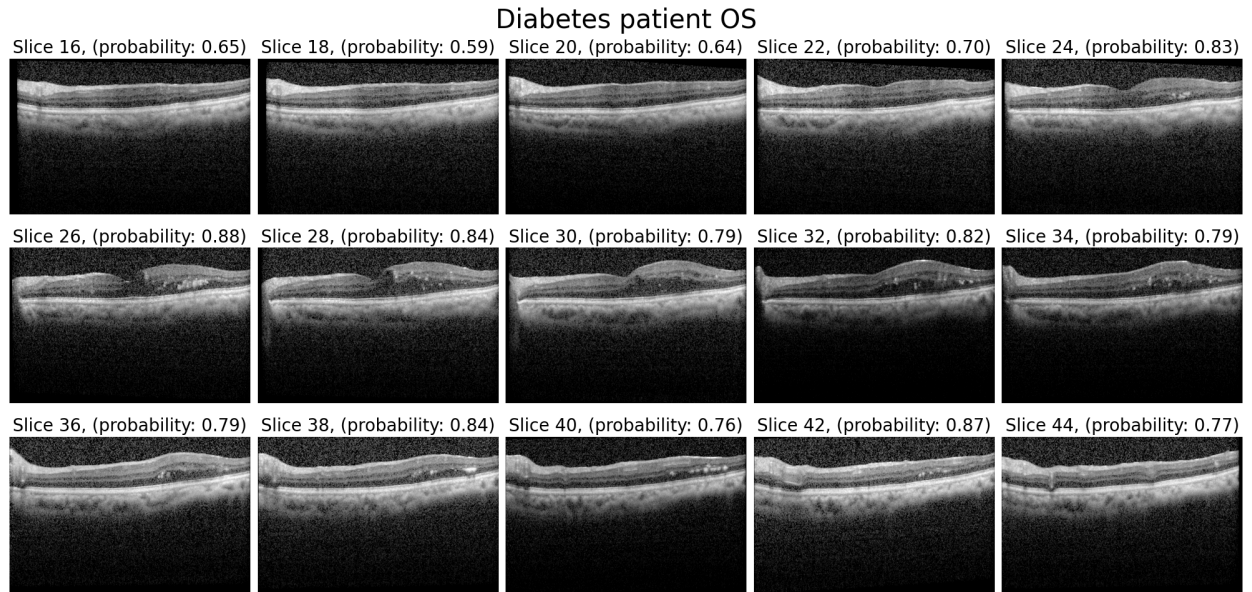
Supplementary Fig. 11 Bar plots comparing OCTCube and competing methods on predicting retinal disease in terms of AUPRC (**a**) and AUROC (**b**) in the cross-dataset setting. OCTCube is trained on UW Ophthalmology dataset while the testing OCT volumes are collected from three other independent datasets. The standard 5-fold cross validation is used, with a train:validation split to be 80%:20%. * indicates the significance level at which OCTCube outperforms the best-competing method, with paired t-test p-value $< 5 \times 10^{-2}$ for *, p-value $< 1 \times 10^{-2}$ for **, p-value $< 1 \times 10^{-3}$ for ***.



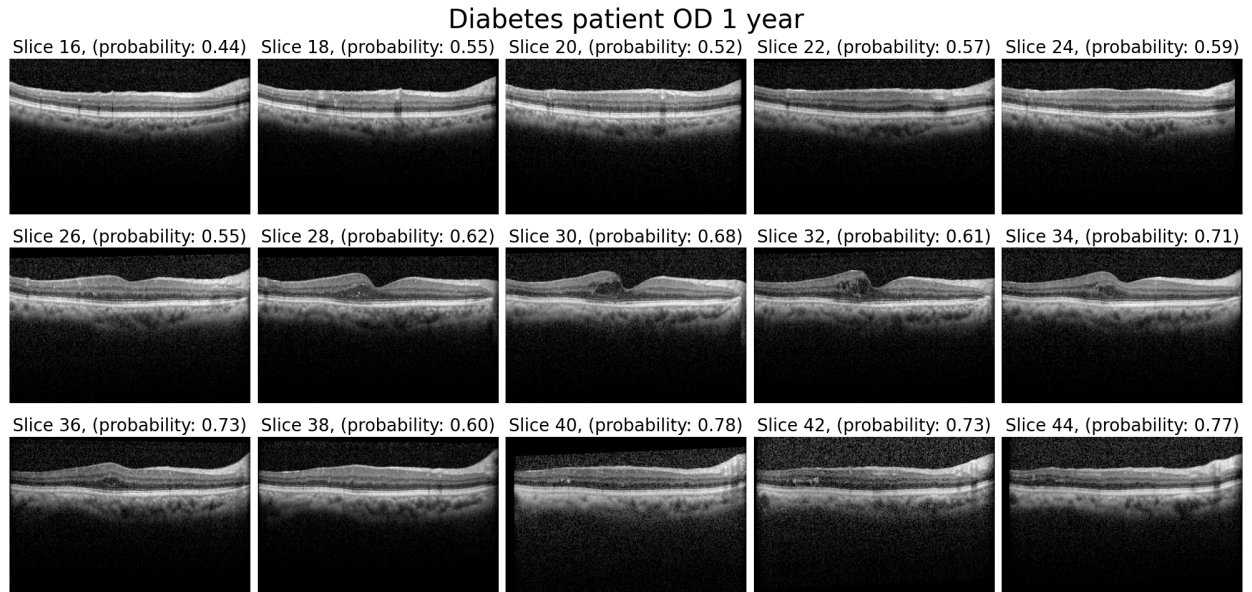
Supplementary Fig. 12 Example OCT slices acquired by Heidelberg Spectralis (a) and Topcon Maestro2 (b) imaging devices. Both OCT volumes are from the same eye of the same patient acquired at the same day in the AI-READI dataset. OCT slices are extracted based on actual pixel spacing and the distance to the center slice. The Spectralis OCT slices have the resolution of (496, 768). The Maestro2 OCT slices have the resolution of (885, 512). The width dimension of Spectralis OCT slices is adjusted for the purpose of visualization.



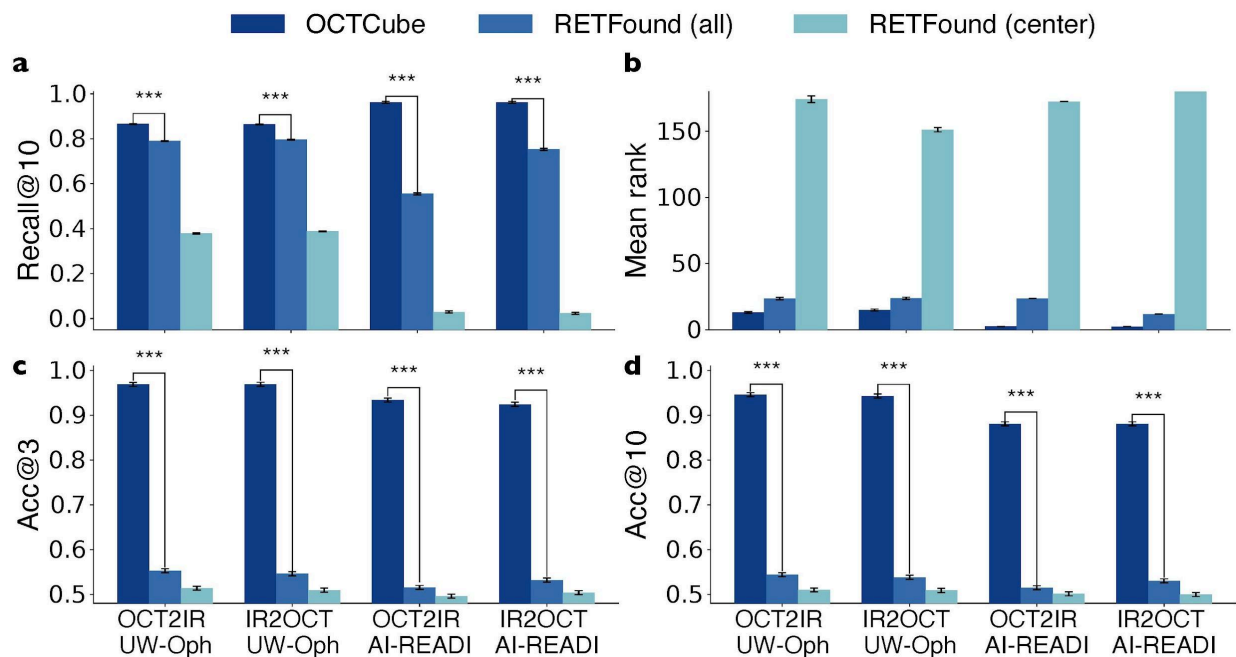
Supplementary Fig. 13 Plots showing the AUROC performance of an aggregation approach predicted probabilities of k slices around the center slices on seven systemic diseases, where k is shown in the x-axis. RETFound, as a 2D approach, corresponds to $k = 0$. The prediction probability is derived using RETFound. The improved performance by considering more slices necessitates the development of 3D models. Plots showing the AUROC performance of an aggregation approach predicted probabilities of k slices around the center slices on seven systemic diseases, where k is shown in the x-axis. The prediction probability is derived using RETFound. The RETFound (center) model, as a 2D approach, corresponds to $k = 0$. Different from directly aggregating predictions, the RETFound (all) model uses a neural network to aggregate features. The improved performance by considering more slices necessitates the development of 3D models.



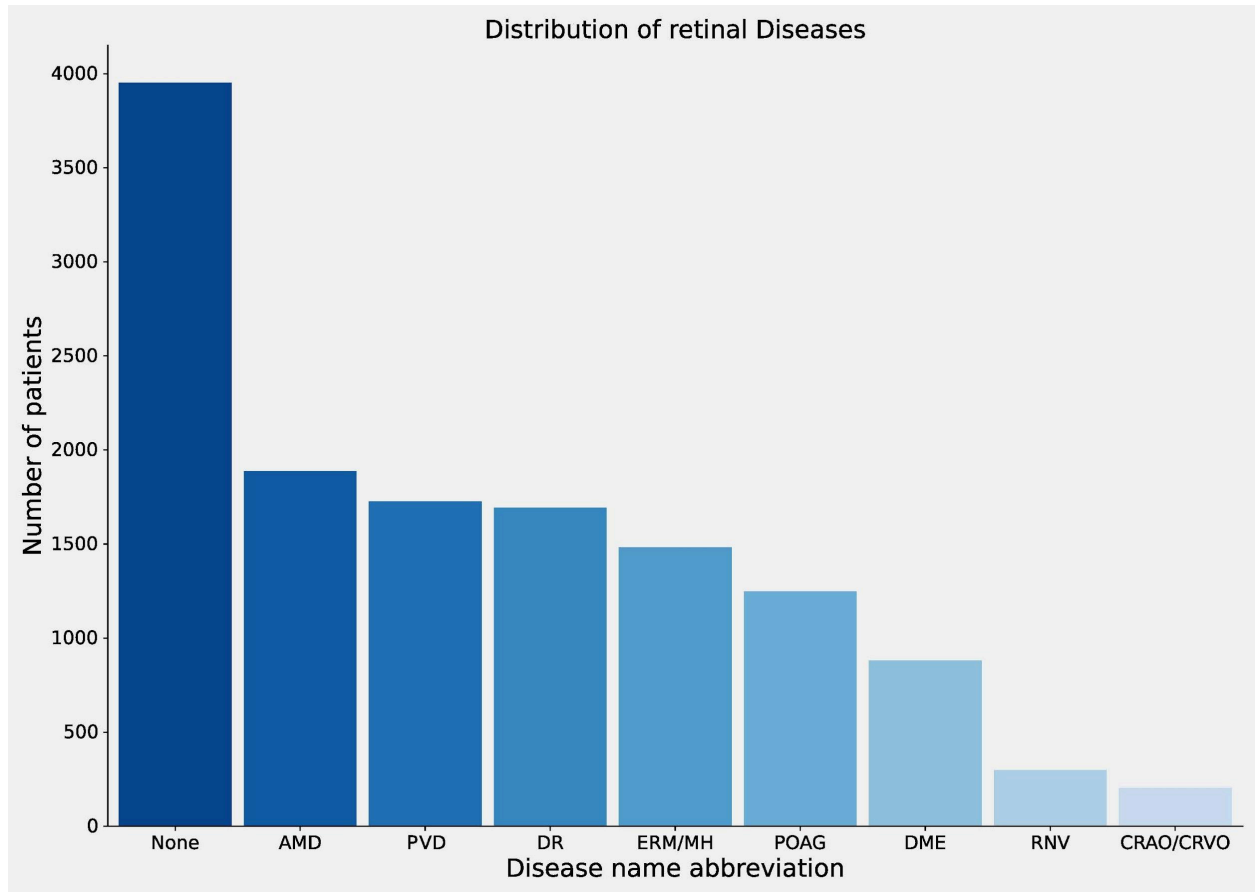
Supplementary Fig. 14 Visualization of OCT slices from the left eye (OS) of the same patient with diabetes studied in **Fig. 4f** acquired on the same day. Slice 26 and 30 are also shown in **Fig. 4g**. Macular edema and hard exudates are more clearly observed in several slices including the center slice compared to **Fig. 4f**. Both OCTCube and RETFound (center) successfully predict diabetes using this OCT volume.



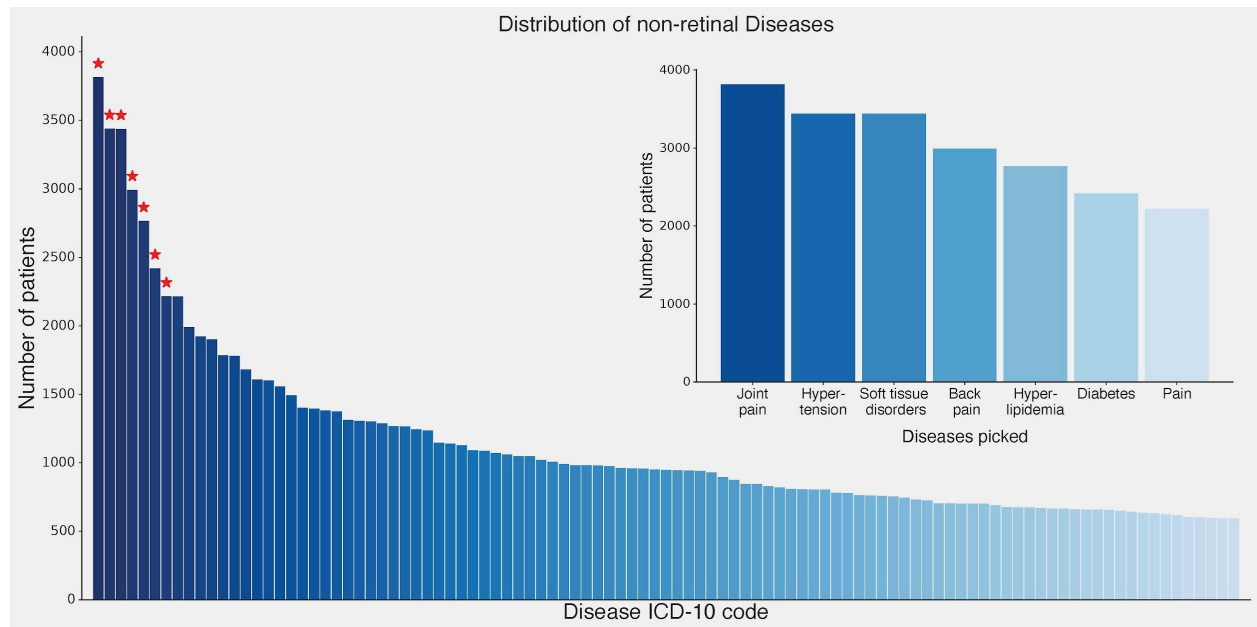
Supplementary Fig. 15 Visualization of OCT slices from the right eye (OD) of the same patient with diabetes studied in **Fig. 4f** acquired after 1 year. Slice 30 and 34 are also shown in **Fig. 4h**. Macular edema and hard exudates are more clearly observed in several slices including the center slice compared to **Fig. 4f**. Both OCTCube and RETFound (center) successfully predict diabetes using this OCT volume.



Supplementary Fig. 16 a-b, Barplots comparing OCTCube and competing methods on cross-modality retrieval on UW Ophthalmology and AI-READI dataset in terms of recall@10 (**a**) and mean rank (**b**) score on OCT to IR retrieval and IR to OCT retrieval. * indicates the significance level at which OCTCube outperforms the best-competing method, with paired t-test p-value $< 5 \times 10^{-2}$ for *, p-value $< 1 \times 10^{-2}$ for **, p-value $< 1 \times 10^{-3}$ for ***. **c-d** Barplots comparing OCTCube and competing methods on cross-modality laterality prediction on UW Ophthalmology and cross-AI-READI dataset in terms of accuracy@3 (**c**) and accuracy@10 (**d**) on OCT to IR retrieval and IR to OCT retrieval. * indicates the significance level at which OCTCube outperforms the best-competing method, with paired t-test p-value $< 5 \times 10^{-2}$ for *, p-value $< 1 \times 10^{-2}$ for **, p-value $< 1 \times 10^{-3}$ for ***.



Supplementary Fig. 17 Disease distribution of retinal disease patients. Barplots showing number of included patients for the retinal disease prediction task. Explicit class imbalance is observed across different retinal diseases. POAG, DME, AMD, ERM/MH, DR, CRAO/CRVO, PVD, RNV denote primary open-angle glaucoma, diabetic macular edema, age-related macular degeneration, epiretinal membrane or macular hole, diabetic retinopathy without macular edema, central retinal vein / artery occlusion, posterior vitreous detachment, and retinal neovascularization respectively.



Supplementary Fig. 18 Disease distribution of systemic disease patients. a, Barplots of the top 100 frequent diseases included in the non-oph disease prediction tasks. Each disease is collected and aggregated based on their level 1 ICD-10 code. **b**, Barplots of the number of patients for the seven selected systemic diseases. M25, I10, M79, M54, E78, E11, G89 refers to joint pain, hypertension, soft tissue disorders, back pain, hyperlipidemia, diabetes, pain. The diseases are selected if their balanced accuracy on the validation set is significantly larger than random guess with $p\text{-value} < 0.001$.

Supplementary Table. 1 Table listing ICD-9 and ICD-10 code of 8 retinal diseases considered in within-dataset retinal disease prediction task. Level 1 code clustered in brackets (e.g., (E08-E11, E13)) indicates the same level 2 code or code series. x denotes any digit between 0-9. Codes linked with '-' indicate consecutive increased digits. POAG, DME, AMD, ERM/MH, DR, CRAO/CRVO, PVD, RNV denote primary open-angle glaucoma, diabetic macular edema, age-related macular degeneration, epiretinal membrane or macular hole, diabetic retinopathy without macular edema, central retinal vein / artery occlusion, posterior vitreous detachment, and retinal neovascularization respectively. Please see Supplementary Table 1 in the uploaded spreadsheet.